LEGACY ACTIVE-SOURCE SEISMIC DATA FOR MODERN 3D TOMOGRAPHY:

INTEGRATING DATA FROM THE MENDOCINO TRIPLE JUNCTION FOR

MULTISCALE IMAGING

by

GABRIEL C. FERRAGUT

A THESIS

Presented to the Department of Earth Sciences
and the Division of Graduate Studies of the University of Oregon
in partial fulfillment of the requirements
for the degree of
Master of Science

September 2021

THESIS APPROVAL PAGE

Student: Gabriel C. Ferragut

Title: Legacy Active-Source Seismic Data for Modern 3D Tomography: Integrating Data from The Mendocino Triple Junction for Multi-Scale Imaging.

This dissertation has been accepted and approved in partial fulfillment of the requirements for the Master of Science degree in the Department of Earth Sciences by:

| | |
|---|---|
| Douglas Toomey, Ph.D | Chair / Advisor |
| Emilie Hooft, Ph.D | Member |
| Diego Melgar, Ph.D | Member |

and

| | |
|---|---|
| Andrew Karduna | Interim Vice Provost for Graduate Studies |

Original approval signatures are on file with the University of Oregon Division of Graduate Studies.

Degree awarded September 2021

THESIS ABSTRACT

Gabriel C. Ferragut

Master of Science

Department of Earth Sciences

September 2021

Title: Legacy Active-Source Seismic Data for Modern 3D Tomography: Integrating Data from The Mendocino Triple Junction for Multi-Scale Imaging

The Mendocino Triple Junction (MTJ) joins the Gorda, Pacific, and North American plates and migrates northward leaving the San Andreas Fault in its wake. This affects subduction-related stress conditions that control megathrust locking, slab window formation, and asthenospheric upwelling at the southern terminus of the Cascadia Subduction Zone (CSZ). These geologic variables impact earthquake hazards and remain relatively poorly understood. Constraining them requires a high-resolution multi-scale 3D seismic imaging approach using local and teleseismic earthquakes as well as active-source data. Yet active-source data near the MTJ is decades old, incomplete, and inconsistent in its metadata. To facilitate future multi-scale seismic imaging of the MTJ, we rescue archived active-source data, resulting in a dataset usable for modern 3D tomography. Forward modelling shows varying but generally high misfit (1ms to >1s), indicating additional structure exists not accounted for in the model, but which may be resolved in future multi-scale inversions.

# CURRICULUM VITAE

NAME OF AUTHOR:  Gabriel C. Ferragut

GRADUATE AND UNDERGRADUATE SCHOOLS ATTENDED:

> University of Oregon, Eugene
> North Dakota State University, Fargo

DEGREES AWARDED:

> Master of Science, 2021, University of Oregon
> Bachelor of Science, Geology, 2012, North Dakota State University
> Bachelor of Science, Physics, 2012, North Dakota State University

AREAS OF SPECIAL INTEREST:

> Geophysics
> Seismology
> Remote Sensing

PROFESSIONAL EXPERIENCE:

> Pathways Intern, USGS, Ongoing

PUBLICATIONS:

> Liu, T., Klemperer, S. L., Ferragut, G., Yu, C. (2019). Post-critical *SsPmp* and its applications to Virtual Deep Seismic Sounding (VDSS) – 2: 1-D imaging of the crust/mantle and joint constraints with receiver functions, *Geophysical Journal International*, Volume 219, Issue 2, Pages 1334–1347, https://doi.org/10.1093/gji/ggz370

TABLE OF CONTENTS

LIST OF FIGURES

LIST OF TABLES

# CHAPTER I:   INTRODUCTION

       The Cascadia Subduction Zone (hereafter, CSZ) has been the subject of extensive research, due in part to the occurrence of large-magnitude, highly destructive earthquakes. The CSZ displays along-strike variations in sediment thickness (Han et al., 2017, 2018; Horning et al., 2016), inferred fluid content (Delph et al., 2018), sub-slab mantle buoyancy (Bodmer et al., 2018), slip deficit (Schmalzle et al., 2014), episodic tremor-and-slip (ETS) (Brudzinksi and Allen, 2007), and seismicity (Bostock et al., 2019), the latter being largely restricted to the northern and southern regions (Fig. 1-1).
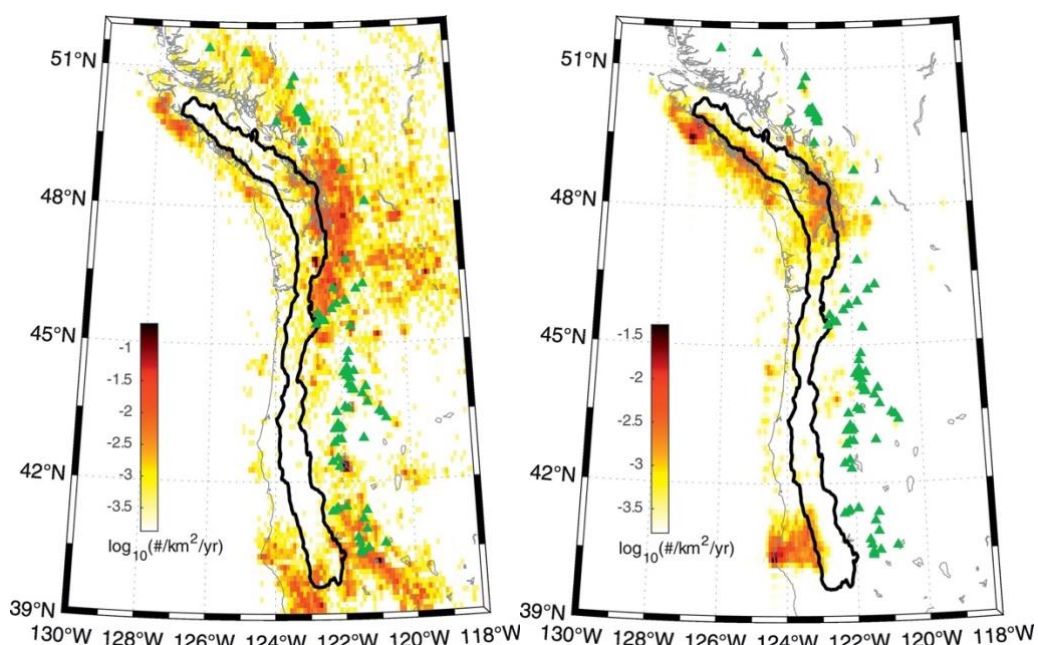


*Figure 1-1: Variations in crustal (left) and slab(right) generated seismicity across Cascadia, modified from Bostock et al., (2019).*

       It is known that fluid content (distribution, pore pressure, and migration) and mantle behavior (buoyancy) may influence megathrust locking and slip behavior, and thus, resulting rupture scenarios (Bodmer et al., 2018; Peacock and Hyndman, 1999). Therefore, a better understanding of the physical and geological factors that control these variables and associated seismicity is an integral component to improved analysis of seismic hazards. Yet the relative lack of detectable seismicity in the CSZ can make constraining these factors difficult. Multi-scale seismic tomography provides an opportunity to create a highly detailed velocity model that images subduction interface

and adjacent upwelling mantle by utilizing the entirety of available data jointly. The detail of such a model will allow for unprecedented constraint of physical parameters (Paulatto et al., 2017) such as slab dip, flexure, mantle buoyancy, fluid distribution and migration, that are thought to control seismicity and megathrust locking in Cascadia.

Despite relative quiescence of the CSZ, the region surrounding the Mendocino Triple Junction (MTJ) is the most seismically active along the margin, yielding denser regional earthquake data. Additionally, the MTJ has been the site of numerous passive array deployments and onshore/offshore active-source experiments (Fig. 4-1, Fig. 4-2). While previous work (Chen et al., 2015) has jointly inverted local earthquakes and teleseisms, no studies have sought to include the legacy active-source data in Cascadia or extended offshore. To address this knowledge gap and progress towards multiscale studies in southern Cascadia we've collected all available legacy active-source data surrounding the MTJ, including over 200,000 first arrival picks. While incomplete, inconsistent, and not readily usable in downloadable format, these data have been collated with available metadata sources to produce a self-consistent seismic dataset compatible with Stingray/TomoLab, a modern 3D tomographic imaging routine capable of utilizing active-source data, regional earthquakes, and teleseismic data jointly.

# CHAPTER II:  GEOLOGICAL SETTING & HISTORY

**Tectonic Setting & History of the MTJ**

For much of the last 200 million years western North America was in a state of continual terrane accretion via the subduction of the ancient Farallon Plate. Approximately 25-30 million years ago (Furlong and Schwartz, 2004; Materna et al., 2018; Henstock and Levander, 2003) the East Pacific Rise, a mid-ocean ridge (MOR) then separating the Pacific and Farallon plates, impinged upon the North America plate. Subduction of this divergent plate boundary resulted in a reorganization of tectonic interactions and the formation of two triple junctions migrating in opposite directions, the Mendocino Triple Junction in the north, and the Rivera Triple Junction to the south (Fig. 1).
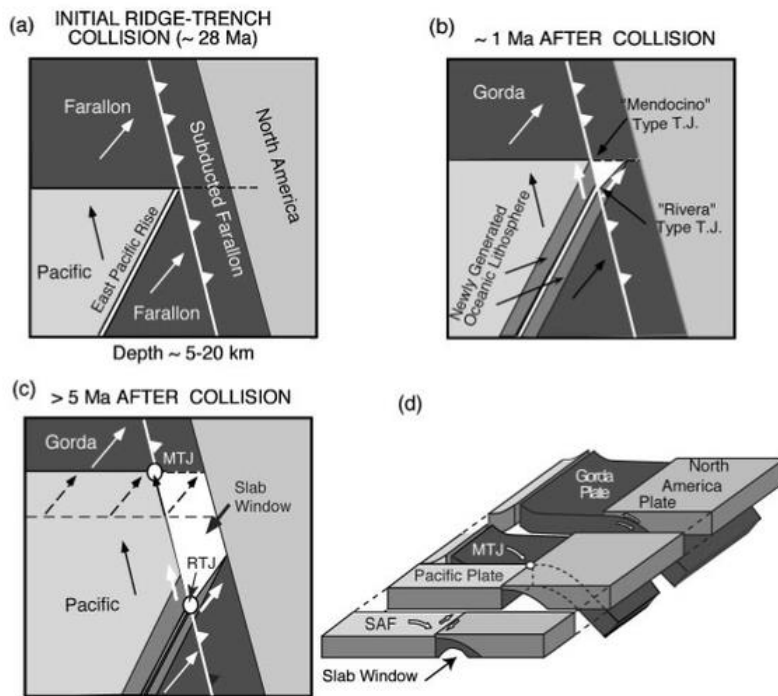


*Figure 2- 1. Conceptual model of the Mendocino Triple Junction formation and subsequent migration creating a slab window in the triple junction wake (Furlong and Schwartz, 2004)*

Between these new junctions a transform regime developed among the northward moving Pacific plate and the western edge of North America, yielding the infant San Andreas Fault. The Farallon plate, now bisected at the surface, continued to be subducted

beyond the northern and southern termini of the new San Andreas, ultimately leading to the modern day Gorda, Rivera, and Cocos plates (Furlong and Schwartz, 2004).

The lithospheric evolution preceding and following MTJ passage is thought to be governed by the so called "Mendocino Crustal Conveyor" (MCC) of Furlong and Govers, (1999). In this model, there is a migrating uplift and subsidence wave due to viscous coupling of the upwelling asthenosphere and continental lithosphere as MTJ migrates northwards, leaving a slab gap in its wake. Such viscous couple and "conveyor" behavior is likely to affect slab flexure, and potentially locking. A substantial change in crustal thickness has been imaged with wide-angle active source data (Beaudoin et al., 1994, 1998) and *P* wave receiver functions (Hayes and Furlong, 2007), however these finds are restricted to 2D profiles. It remains unknown to what degree sub-slab buoyancy and mantle flow (Bodmer et al., 2019) may interact with viscous coupling that is thought to drive the migrating triple junction and associated crustal deformation.

**Regional Seismicity**

Unsurprisingly, the complexity of triple junction migration, subducting oceanic lithosphere, and a growing San Andreas Fault yield a high degree of earthquake activity around Cape Mendocino. Earthquake catalogs retrieved from IRIS and the Northern California Earthquake Datacenter (NCEDC) reveal more than 80,000 small to moderate magnitude events regionally since 2000 (Fig. 2-2)
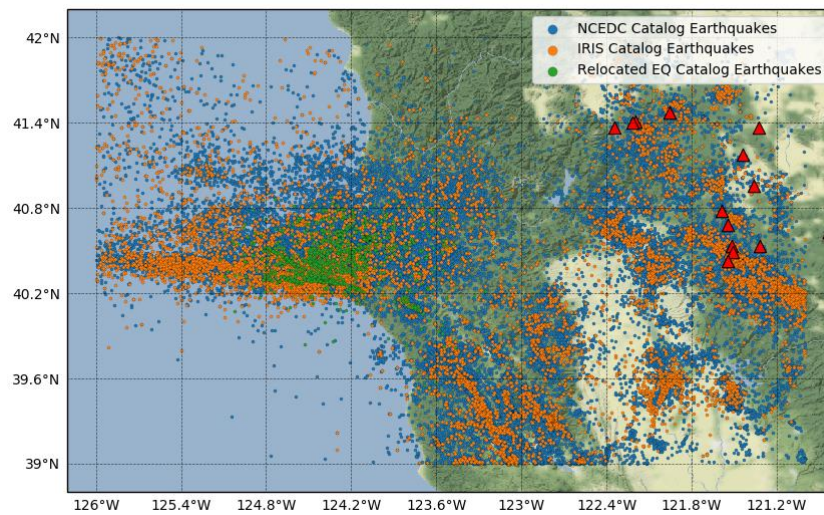


*Figure 2-2 Aggregated earthquake catalogue results for the Northern California Earthquake Data Center (NCEDC), the Incorporated Research Institutions for Seismology (IRIS) and a regional subset of relocated earthquakes. Volcanoes shown in red.*

# CHAPTER III: PREVIOUS WORK

The Mendocino Triple Junction has been a target of seismic imaging efforts for decades. The relative abundance of earthquakes in southern Cascadia has provided data for many earthquake tomography studies but there are relatively few published works devoted to imaging the triple junction in high-resolution or in 3D. The Mendocino Triple Junction Seismic Experiment (MTJSE) is the richest supply of controlled-source seismic data in southern Cascadia, and it generated a number of publications as a result. Below is a summary of previous seismic imaging studies, for more detail see Tables A-5 and A-6.

Local earthquake tomography has been used to image the MTJ several times such as the work of Verdonck and Zandt (1994), who produced an estimate of three-dimensional crustal velocity structure, but at a coarse resolution of 5km. Even very recent publications like Guo et al., (2001) perform tomographic inversions with local earthquake data but are limited to a similarly coarse resolution.

To produce higher resolution velocity models, denser data with precisely known origins and timing is required, which the active-source MTJSE facilitated. Beaudoin et al., (1994) used the first of the MTJSE data gathered in an array calibration piggyback experiment to forward and inverse model reflectors in the crust interpreted to be the Gorda slab. Beaudoin et al., (1996) imaged the slab gap using the data collected in the 1993 onshore portion of the MTJSE. Gulick et al., (1998) analyzed multichannel seismic reflection data from the MTJSE across four profiles to investigate the accretionary prism at the most southern extent of the Cascadia Subduction Zone (CSZ). The same year, Beaudoin et al., (1998) analyzed N/S trending 2D data from the onshore survey to image the transition from subducting slab to slabless window. Hole et al., (2000) produced a 3D

velocity model by inverting first arrival times from the 1994 onshore 3D array of the

MTJSE. The data collected simultaneously by the 2D onshore lines and offshore OBSs in

1994 was used by Henstock and Levander (2003) to produce crossing 2D velocity models

yielding a rough idea of 3D structure.

# CHAPTER IV: LEGACY SEISMIC DATA

## Overview

The Mendocino Triple Junction has long been a region of seismic and geophysical interest due not only to the abundant seismicity, the complexity of triple junction tectonics, and the intellectual merit studying them carries, but also because it is the transition zone between two distinct regimes of plate motions that produce vastly different stress conditions that subsequently control the major seismic hazards threatening human populations on the west coast of the United States. These tectonic boundaries are the Cascadia Subduction Zone (CSZ) north of the MJT, and the San Andreas Fault transecting California to the south. While these regimes are distinct, they may also influence one another during rupture scenarios (Goldfinger et al., 2008) heightening the importance of constraining both Earth structure as well as other physical conditions that may impact potential rupture scenarios such as presence of fluids, plate coupling, and stress conditions.

## Community Interest: Utilizing Legacy Data

Recently, a general effort has been undertaken by the seismological community to collect, collate, and modernize the abundance of seismic data collected in decades prior that has hitherto gone under-utilized. Much of these data remain inaccessible, and the data that is available may be missing associated metadata critical to its continued usability. Community workshops in partnership with consortiums like Incorporated Research Institutions for Seismology (IRIS) have sought to remedy this by collating and hosting widespread legacy seismic data and metadata in adherences to FAIR (Findable, Accessible, Interoperable, and Reusable) standards (Hwang et al., 2020), while new international open-access efforts like the Seismic Data Repository (SeisDARE) have collated data for specific regions and scales of investigation, such as the Iberian continental lithosphere (DeFelipe et al., 2021) Additionally, the application of new data-mining techniques to legacy seismic data has generated interest within the context of national defense, with the U.S. Department of State recently calling for funding proposals using legacy data in explosion monitoring research (DOS, Broad Agency Announcement, 2021). While uncertainties and inconsistencies are common in these data sets, their

integration into a modern seismological framework presents a worthwhile endeavor in the process of refining our understanding of tectonic interactions and seismic hazards not only in Cascadia, but globally.

**Active-Source Data**

      In the last five decades numerous controlled-source seismic experiments have taken place in along the CSZ, totaling nearly 40 million ray paths (Table A-4), but only a handful have been dedicated to exploring onshore/offshore structural variations in southern Cascadia near the Mendocino Triple Junction.
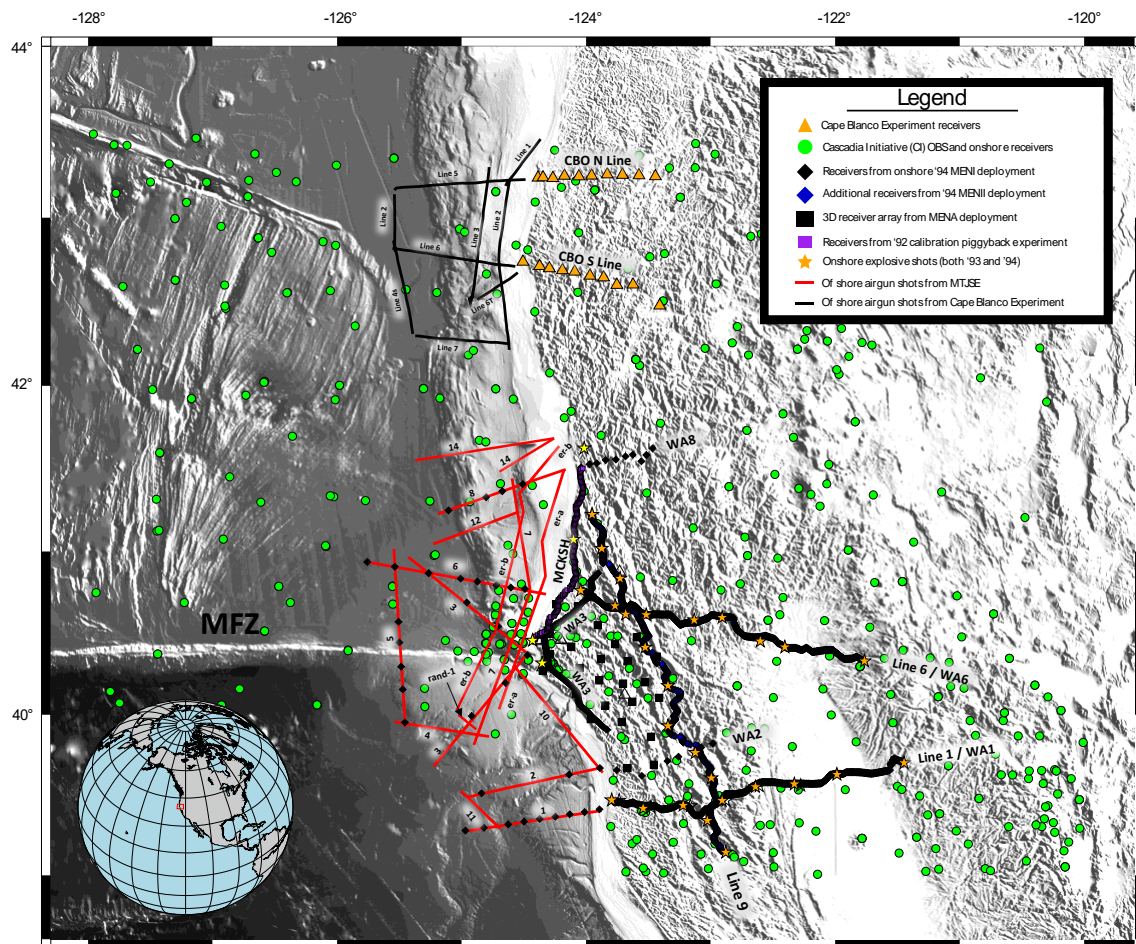


*Figure 4-1: Legacy active-source seismic experiments in the region of the Mendocino Triple Junction (MTJ) over the course of the last three decades.*

      Two experiments provide wide-angle geometries suitable for imaging the crust in detail. The 1994 Mendocino Triple Junction Seismic Experiment (MTJSE), discussed in detail later, was a multi-phase mixed source experiment centered on the triple junction

itself. To the north, the Onshore/Offshore Wide-Angle Seismic Recording at Cape Blanco (CBO) is situated at a suspected crustal shear zone.

## Passive-Source Data

In addition to active-source data, the western margin of North America has been host to many passive seismic arrays, both permanent and transient. Permanent networks like the Pacific Northwest Seismic Network (PNSN), the Berkeley Digital Seismic Network (BDSN), and the Northern California Seismic Network (NCSN) all provide rich sources of data for onshore recording of local, regional, and teleseismic earthquakes.
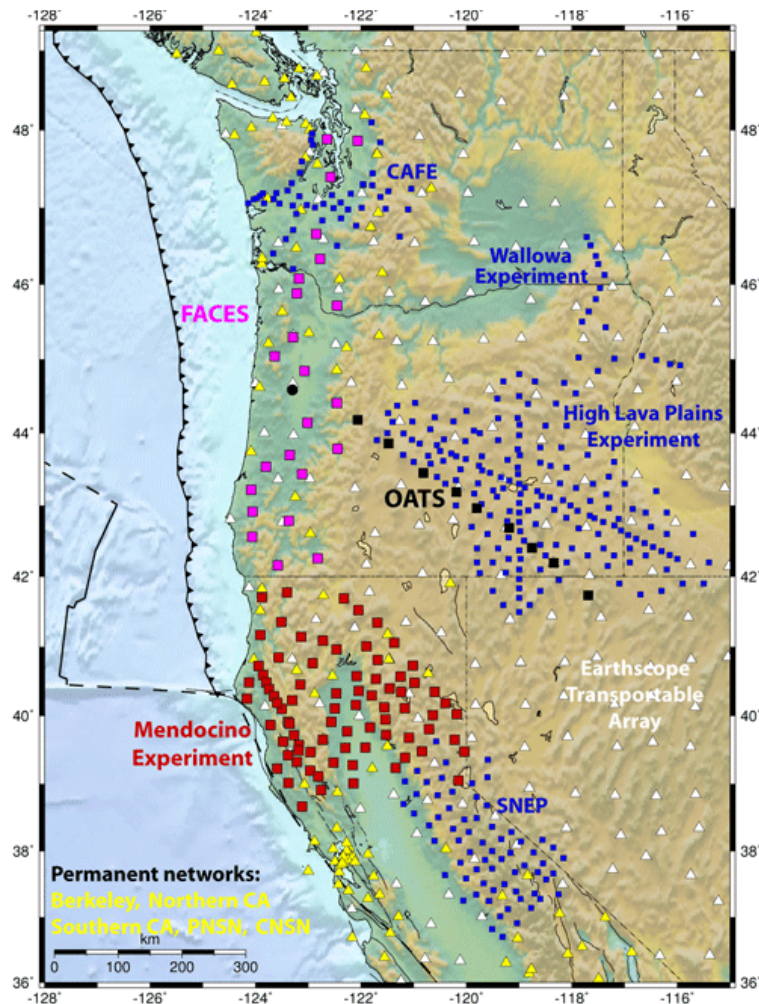


*Figure 4-2: Recent transient seismic arrays deployed in the Pacific Northwest and Northern California, not including the more recent onshore/offshore deployment of the Cascadia Initiative (Toomey et al., 2014). Modified from FlexArray Deployments in the Pacific Northwest, Retrieved August 15 2021, from http://seismo.berkeley.edu/~rallen/research/cascadia/flexmap.php*

Transient array experiments like the well-known Transportable Array (TA) have also offered supplementary coverage to the permanent networks. Alongside the TA, more targeted experiments like the Flexible Array Mendocino Experiment (FAME) provide improved receiver spacing and denser data collection at the MTJ. Amphibious seismic array deployments such as the Cascadia Initiative (CI) have even supplied array coverage spanning from offshore to onshore, allowing for better relocation of local earthquakes and improved usability in seismic studies.

# CHAPTER V:  DATA DESCRIPTION & PROCESSING

## Data Search

| Active Source Data | | |
|---|---|---|
| Experiment Name | Data Repository | Data Report # |
| MENI | IRIS DMC | 96-018 |
| MENII | IRIS DMC | 96-017 (incomplete) |
| MENA | IRIS DMC | 96-008 |
| MENDO | IRIS DMC | 98-005 |
| MCKSH | IRIS DMC | 94-004 |
| CBO | IRIS DMC | 95-003 |

*Table 5-1: Available archived datasets and data reports near the Mendocino Triple Junction.*
*Note that data report 96-017 is incomplete as downloaded from the IRIS DMC.*

To assess the density of existing data and suitability for integrated use in southern Cascadia it was first necessary to identify, as completely as possible, all seismic experiments that have occurred in the region (Fig 5-1; Fig 5-2). This was achieved through a combination of literature research and collaboration with both USGS personnel and principal investigators of previous experiments throughout Cascadia (Trehu and the Mendocino Working Group, 1995). The Incorporate Research Institutions for Seismology (IRIS) maintains a repository for the data products and results of seismological experiments and campaigns for the use of the scientific community at large that houses many archived datasets (Fig 5-1; Fig 5-2).

| Experiment Name | No. Files | Horz. | Vert. | Other |
|---|---|---|---|---|
| MENI | 17 | 8 | 4 | 3 (co-loc stations) |
| MENII | 39 | 21 | 17 | 1 (no comp, just WA3_.segy) |
| MENA | 26 | 0 | 26 | N/A |
| MENDO | 18 | - | - | 1 ".nav" file |
| MCKSH | 1 | 0 | 1 | N/A |
| CBO | 18 | 0 | 18 | N/A |

*Table 5-2: Contents of archived datasets available via the IRIS DMC and approximate estimations of data completeness in terms of available files and data components.*

## Data Archiving and Conversion

Correspondence with the IRIS DMC indicates that as of late 2018 IRIS underwent an effort to modernize their data archives by converting some existing physical data storage media such as seismic data on Digital Audio Tapes (DAT), Digital Linear Tapes (DLT), and Exabyte tape drives to newer electronic formats that are more readily accessible and reliably maintained and phasing out the hosting of said physical data and the tools necessary to read it. As a result, the original data tapes archived at IRIS are no longer in existence to the best of our knowledge. There remains some possibility that experiment PIs have the retained copies of these data, but personal communication with several investigators (Anne Trehu, Bruce Beaudoin, and John Hole) has not yielded such.

## Data Formatting

### SEG-Y

Archived datasets hosted at the IRIS DMC are generally available in either of two formats, SEG-Y or PH5, with older experiments typically stored as the former. All data discussed below was originally submitted to IRIS in the SEG-Y format. SEG-Y is a binary file format developed by the Society of Exploration Geophysicists (SEG) as an open standard for storing active-source seismic data and has been in use for nearly 50 years (Barry et al., 1975). The binary file consists of file headers, trace headers, and trace data, each occupying a predefined number of bytes. Since its original form, *rev 0*, SEG-Y has undergone two other revisions expanding its usability, one in 2002 (*rev 1*) and another more recently in 2017 (*rev 2*). Common to all revisions is a 3200-byte EBCDIC or ASCII file header, a 400-byte binary file header, and data traces up to $2^{16}$ data traces ($2^{32}$ for *rev 2*) each with a 240-byte trace header. For information on character encoding or specific differences in SEG-Y revisions (Fig. A-1).

While it remains a popular format for data storage, particularly in industry, datasets are frequently converted into SEG-Y format with metadata stored in non-standard byte locations, with significantly customized headers, or simply with missing information. This variability necessitates careful review of format specifics when collating multiple datasets. The MATLAB-based data plotting and picking software tlPicker (developed by William Wilcock of the University of Washington) and which

functions alongside Stingray/TomoLab (developed by Douglas Toomey of the University of Oregon), provides functionality for reading SEG-Y. Additionally, many open-source Python libraries, frameworks, and dedicated packages exist to facilitate reading and writing of SEG-Y files (Table 5-3). The scripts accompanying the dataset compiled here make extensive use of two:

| Package | Language | Description |
|---------|----------|-------------|
| ObsPy | Python | General framework for processing, plotting, and cataloging seismological data. |
| SEGYSAK | Python | Dedicated SEG-Y package for input/output, plotting, analysis, manipulation, and conversion |

*Table 5-3: Python-based packages for reading, writing, and manipulating time series data, particularly when formatted in the standardized SEG-Y data format of the Society of Exploration Geophysicists.*

## Available Data

When these data were initially collected in the 1990s, they were processed into shot and receiver gathers using standard data processing tools of the time such as *ref2segy* and *segygather*. A summary can be seen in Table 5-4.

| Phase | 2D/3D | On/Off | No. Shots | Shot Spacing | Source (BE, AG) | No. Stations | Station Spacing | Data gather |
|-------|-------|--------|-----------|--------------|-----------------|--------------|-----------------|-------------|
| MENI | 2D | Onshore | 27 | 2500m | BE | ~ 600 per line | 0.35 - 0.40km | shot |
| MENII | 2D/3D | On/off | 2/35765* | 50 – 125m | AG, BE | ~ 500 per line | 0.01 – 10km | both |
| MENA | 3D | On/off | 35765 | 50m | AG | 26 | ~ 10km | rcvr |
| MENDO | 2D/3D | Offshore | 35765 | 50m | AG | 22 | | rcvr |
| MCKSH | 2D | Onshore | 4 | 510-1000m | Borehole BE | 200 | 0.5 – 1km | shot |
| CBO | 3D | On/off | 12283 | 50m | AG | 18 | 9km | rcvr |

*Table 5-4: Experiment geometry, coverage, source type, data gather conventions, and source/receiver spacing for the various phases of the Mendocino Triple Junction Seismic Experiment (MTJSE) and the Cape Blanco Onshore/Offshore seismic recording (CBO). Sources are borehole explosive (BE) and airgun (AG). *Two land shots were fired in addition to airgun sources*

Many, but not all, of the reports describing these datasets provide ample information concerning how this process was conducted. Unfortunately, the content and formatting of the data in its now available electronic forms appears to conflict with the documentation describing the original physical tapes. The most consistent issues we faced in analyzing these data were missing components (chiefly horizontals) from 3-

component receivers, entirely absent data files for certain stations. Additionally, while intended to adhere to a standardized PASSCAL SEG-Y header format, we have found that trace information is sometimes repeated, missing, stored in incorrect byte locations, or occasionally just wrong.

That said, much of the available data appears to be of high-quality with extractable experiment geometry and timing, and thus still represents a rich source to incorporate into seismic studies in southern Cascadia. Vitally, the cutting and resampling of the traces gathered in the SEG-Y files remains consistent and correctly recorded in each trace header.

## MCKSH

In 1992 a series of test shots were fired by the USGS to aid in seismic array calibration in the vicinity of the MTJ. These shots were also intended to act as an initial pilot experiment for the future Mendocino Triple Junction Seismic Experiment (MTJSE). A piggyback experiment was conducted to utilize these shots. A line of 200 receivers, 60 of which recorded radial and transverse components in addition to the vertical, were deployed roughly parallel to the coast at and spanning 140km from Cape Mendocino northward to approximately 41.5° N. A total of four shots were detonated in boreholes along this line. The data was cut and merged into shot gathers.

## MENI (MEN-1)
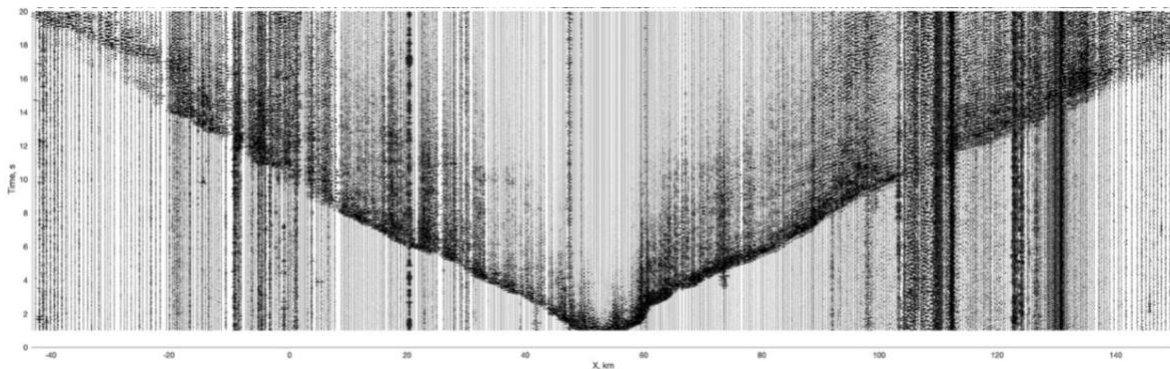


*Figure 5-1: Shot gather from the onshore portion of the MTJSE in 1993. Source type is a borehole explosive, recorded by receivers in a 2D geometry. The X-axis displays two variables. The bottom labels show the position in X of the recorded trace, where X is on a cartesian model grid. The upper labels show source/receiver offset.*

In 1993, the start of the main experiment began with the deployment of 3 large-aperture onshore lines of seismometers referred to as Line 1, Line 6, and Line 9 (Table 5-5). The orientations of these lines are constructed such that 2D refraction profiles (Fig. 5-1) will cross-sect features of interest at the MTJ (Fig. 4-1). Line 1 is trends E-W and lies south of the MTJ starting at the coast near Ft. Bragg and transecting the Macama Fault, Bartlett Springs Fault, and northern Central Valley before terminating at Lake Oroville. Line 6 is oriented approximately in the down-dip direction of the subducted Gorda slab and sits north of the MTJ extending from Eureka, CA to Lassen Peak. Line 9 is roughly coast-parallel and extends from Redwood National Park southward to Clear Lake, crossing the inferred southern edge of the subducted slab and targeting the region of transition from slab to slabless.

| Line Name | Line Length | No. Receivers | Receiver Spacing | No. Shots | Shot Spacing |
|---|---|---|---|---|---|
| Line 1 – E/W | ~200 km | 571 | 0.35 km | 8 | 25 km * |
| Line 6 – E/W | ~200 km | 566 | 0.35 km | 8 | 25 km * |
| Line 9 – NW/SE | ~250 km | 556 | 0.40 km | 11 | 25 km |

Table 5-5: Experiment geometry characteristics for the 1993 onshore portion of the MTJSE. *Shots 101 and 102 have a 45km spacing, shots 601 and 602 have a 55km spacing

Receiver locations from this initial onshore portion of the experiment are published in the USGS Open-File Report 95-275. To check for consistency and accuracy, these metadata were digitized directly from the report and compared metadata sources provided by third parties involved in the initial experiment and provide a reliable source for location data (Anne Trehu, John Hole, Tom Brocher, pers. comm.). Data in shot gathers contains differing numbers of receivers as compared to the original documentation (Table 5-6).

| Line Name | No. Receivers Documented | No. Receivers in Data |
|---|---|---|
| Line 1 – E/W | 571 | 573 |
| Line 6 – E/W | 566 | 573 |
| Line 9 – NW/SE | 556 | 381 |

Table 5-6: Discrepancy between documented receivers in 2D seismic lines of the 1993 onshore experiment (MENI) compared to number of receivers present in shot gathered SEG-Y data available for download via the IRIS DMC.

## MENII (MEN-2)

The following year in 1994, the experiment conducted its second phase in which two of the large-aperture lines of the previous onshore experiment (Line 1 and Line 6) were extended offshore using ocean bottom seismometers (OBS) to create a wider aperture seismic line. This expansion to an onshore/offshore experiment allows for ray coverage spanning the transition from the Pacific Plate to the North American Plate across the San Andreas Fault in the south (Line 1).

| Line Name | No. Receivers | Receiver Spacing | No. Shots | Shot Spacing |
|---|---|---|---|---|
| WA1 | 121 | 1 km | 754 | 125m* |
| WA2 | 8 | 10 km | 1904 | 50m |
| WA3 | 128 | 1 km | 4125 | 50m |
| WA6 | 129 | 1 km | 2468 | 50m |
| WA8 | 10 | 6 km | 1808 | 50m |
| High Density Array | ~200 | 33 – 66m | 2 | NA |

*Table 5-7: Source/receiver spacing and numbers for the onshore/offshore lines of the 1994 MENII phase of the MTJSE. Coordinates for sparse lines (WA2, WA8) available in the Appendix and in associated Github repository (Ferragut, 2021).*

Experiment geometry can be seen in Figure 4-1 and shot/receiver spacing information in Table 5-7, with additional information in the Appendix. In addition to the reoccupied new wide-angle lines (WA1, WA6, WA9) several new lines (WA2, WA3, WA8) were deployed to maximize array coverage and target the center of the triple junction itself. Two of these lines (WA2 and WA8; Table A-5-6) are sparsely instrumented while a third (WA3) is of similar spacing to the reoccupied lines. The majority of the 1994 deployment was designed to record offshore airgun shots, a high-density array near Lake Pillsbury was constructed and intended to record two onshore shots detonated at the site of previous deployment's shotpoint 106 (SP106).

## MENA

In conjunction with the onshore wide-angle lines and the offshore sources from the R/V *Ewing*, an array of receivers was set up in the center of the experiment to evaluate 3D structure of the subducting Gorda slab. In total, 24 3-component stations were deployed and continuously recorded the ~36,000 airgun shots from offshore. The

archived dataset is complete for vertical component data, but all horizontal component data appears to be missing. Data is collected in receiver gathers, with each SEG-Y file corresponding to a single station. In general data quality appears good and arrivals are quite often apparent at offsets greater than 100km. Smaller offset ranges qualitatively exhibit a better signal-to-noise ratio and are more likely to have pickable secondary phase arrivals (Fig 5-2). This 3D array is by far the most densely picked portion of the dataset, but primarily first arrivals were picked.
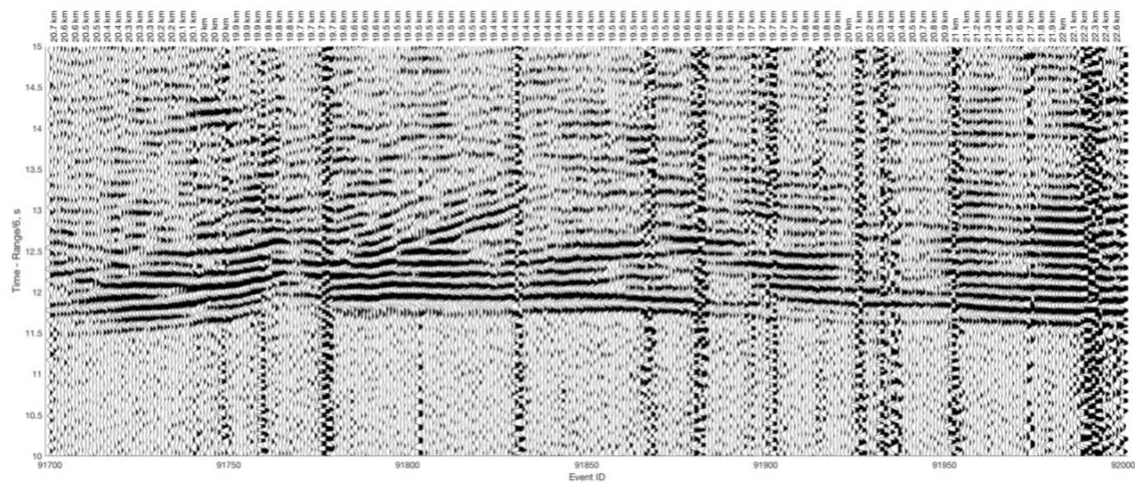


*Figure 5-2: Example of high-quality data recorded at a station in the onshore 3D array. First arrivals are clear and coherent. Some secondary arrivals are evident and could be picked with the aid of forward modelling. The X-axis displays two variables. The bottom labels show the airgun shot ID corresponding to each trace. The upper labels show the source/receiver offset, in this case shots are recorded in a fan geometry, with offset being approximately equal for all data.*

       The PASSCAL data report for the MENA dataset provides an outline of how shot identification numbers are assigned. These identification numbers are referred to differently across both data reports and SEG-Y header labels. These values are often reported "Field File Identification" or "Field File Number", abbreviated as "FFID". This is a convention utilized in the SEG-D data format. The SEG-Y convention, and the labeling that I/O tools use, refers to this as "Original Field Record". To create unique IDs for each airgun line, MENA data alters the convention of the offshore cruise (MENDO) by adding static scale factors. In total, 25 ship tracks are identified in both the reported information and in the SEG-Y headers of the onshore 3D array. This differs from the data report of the offshore cruise, which only shows 19 ship tracks (see below).

| SEG-Y Derived MENA Airgun Shot IDs | | | |
|---|---|---|---|
| Line | Reported Shots in Line | Apparent Shot ID Range | Apparent Shots in Line |
| MCS-1b | 1439 | 10151:11589 | 1439 |
| MCS-1c | 627 | 20137:20763 | 627 |
| WA-1 | 747 | 30101:30854 | 754 |
| MCS-11 | 755 | 40100:40854 | 755 |
| MCS-10a | 768 | 50100:50867 | 768 |
| MCS-2 | 1904 | 60100:62001 | 1902 |
| MCS-10 | 1167 | 70868:72036 | 1169 |
| MCS -7 | 436 | 80098:80533 | 436 |
| MCS -7a | 3353 | 90100:93453 | 3354 |
| er-bna | 1014 | 100099:101113 | 1015 |
| MCS-12 | 1224 | 110090:111246 | 1156 |
| MCS-3 | 4124 | 120100:124225 | 4126 |
| MCS-4 | 1325 | 130100:131424 | 1325 |
| MCS-5 | 1511 | 140100:141617 | 1518 |
| MCS-8 | 1808 | 150110:151917 | 1809 |
| er-ana | 1791 | 160103:161892 | 1791 |
| WA-6a | 952 | 170116:171067 | 953 |
| MCS-6a | 2469 | 180100:182568 | 2469 |
| er-as | 2103 | 190100:192202 | 2103 |
| rand-1 | 237 | 200667:200903 | 237 |
| er-bs | 2988 | 210100:213087 | 2988 |
| MCS-7b | 473 | 220100:220572 | 473 |
| MCS-13 | 819 | 230100:230918 | 819 |
| MCS-14 | 1816 | 240109:241924 | 1816 |

*Table 5-8: Number of shots documented in the MENA data report compared to data-derived shot ID numbers and the apparent number of shots per line.*

## MENDO

During the 1994 campaign the R/V *Ewing* supplied airgun shots at sea to be recorded by the onshore arrays and lines discussed above. As an extension of the onshore lines, the R/V *Ewing* also deployed ocean bottom seismometers (OBSs) to record these shots. The PASSCAL data report lists 19 separate airgun lines, most of which record multichannel seismic data (MCS) in addition to supplying sources for onshore and ocean-bottom receivers. Several lines present in the MENA data report aren't presented in MENDO report, such as er-ana, er-as, rand-1, MCS-14, and MCS-14.

| Reported MENDO Airgun Shot IDs | | | |
|---|---|---|---|
| **Line** | **First Shot ID** | **Last Shot ID** | **Shots in Line** |
| MCS-1b | 151 | 1594 | 1444 |
| WA-1 | 100 | 854 | 755 |
| MCS-1c | 137 | 763 | 627 |
| MCS-11 | 100 | 854 | 755 |
| MCS-2 | 100 | 2001 | 1902 |
| MCS-10a | 100 | 867 | 768 |
| MCS-10b | 868 | 2036 | 1169 |
| MCS-7 | 98 | 533 | 436 |
| MCS-7a | 100 | 3453 | 3354 |
| MCS-Bn | 99 | 1113 | 1015 |
| MCS-12 | 109 | 1246 | 1138 |
| MCS-3 | 100 | 4225 | 4126 |
| MCS-4 | 100 | 1424 | 1325 |
| MCS-5 | 100 | 1617 | 1518 |
| MCS-8 | 110 | 1917 | 1808 |
| MCS-An | 104 | 1892 | 1789 |
| WA-6 | 116 | 1067 | 952 |
| MCS-6 | 100 | 2568 | 2469 |
| MCS-As | 100 | 1832 | 1733 |

*Table 5-9: Original shot ID ranges documented in the MENDO data report and the resulting number of shots per line. Static adjustments to shot IDs to create unique values for each survey line are not applied here, only in the MENA data report Note that the number of lines here is also smaller.*

The archived dataset from the IRIS DMC for this offshore portion is unfortunately missing a large proportion of data, presumably due to issues with conversion to electronic formats or physical tape integrity outlined earlier (Table 5-10).

| **Receiver** | **Experiment Line** | **Channels** |
|---|---|---|
| OBS 14 | mcs-3 | 2 |
| OBS 15 | mcs-3 | 2 |
| OBS 18 | mcs-3 | 2 |
| OBS 20 | mcs-3 | 4 |
| OBS 23 | mcs-3 | 4 |

*Table 5-10: Ocean Bottom Seismometers (OBS) from the offshore MENDO portion of the MTJSE. These are a subset of the full experiment, as not all data files are present in the archived dataset.*

## Seismic Phases & Existing Traveltime Picks

One of the most useful aspects of integrating legacy seismic data into updated datasets and modelling workflows is the potential to utilize an abundance of pre-existing travel time picks from previous efforts. We've obtained >200,000 travel time picks from

the '94 MTJSE 3D array via the tomographic work of Hole (2000) as well as a smaller set of unpublished first and secondary arrival picks for the 3D array, '93 MTJSE wide-angle lines, and '94 Cape Blanco onshore/offshore experiment, through collaboration with Tom Brocher of the USGS.

Our current traveltime dataset is intended as a baseline to be integrated into a larger multiscale tomography problem that incorporates local and teleseismic earthquakes. These active-source data individually provide good initial constraints on crustal scale structure, as outlined in previous literature, but have yet to be used fully in an integrated study. In particular, the incorporation of S-wave travel time picks can yield Vp/Vs measurements along the megathrust interface, yielding vital constraints on fluid presence and thus locking distribution and potential rupture scenarios (Guo et al, 2021).

While the archived datasets we compile here are not completely intact, often missing transverse and radial components, a portion of these data still exist and may be used to pick traveltimes. The data structures & models presented here may be used to ray-trace and predict traveltimes of P and S-wave phases to aid in this picking. An important consideration in this process is frequency content and time-energy evolution, as S wave arrivals in horizontal components are often quite easily obscured by noise. This is particularly true near Cape Mendocino, where the local lithology is a complex interplay of accreted sedimentary units that make up the Franciscan Complex (Krohe, 2007).

Below are spectrograms of two traces from the 1993 2D data (Fig. 5-3). The left displays high SNR and an impulsive arrival with little energy recorded beyond the first P wave. By comparison, the right shows a nearby trace of differing ray parameter that shows more complex arriving energy, and while noise is somewhat higher, this trace is more likely to yield secondary arrivals. We include tools to generate these spectrograms in the code package available via Github (Ferragut, 2021).
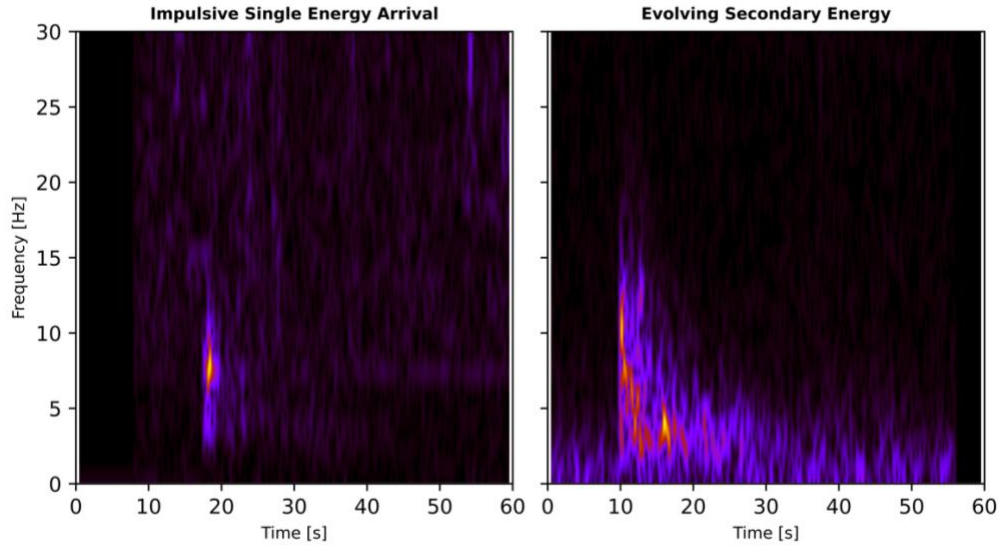
*Figure 5-3: Spectrograms showing a comparison of frequency content through time between two recorded data traces at a seismograph. Each trace corresponds to a seismic source (airgun shot) at a different location. Sedimentary and velocity structure beneath the offshore shot and onshore receiver, as well as ambient noise conditions, impact the resultant energy recorded.*

<u>**Data Processing**</u>

## Topography & Bathymetry

One of the more important elements in ray tracing and tomographic inversions using Stingray and TomoLab, and one that is often not well represented in other comparable 3D tomography codes, is the inclusion of fine-scale elevation models from which the model nodes are then hung, allowing velocity models to exhibit a high degree of fidelity with actual Earth structure. Some velocity models discussed below were constructed utilizing bathymetric or topographic data, in particular the bathymetry from the ETOPO1 dataset (Bell et al., 2016; Amante and Eakins, 2009). The ETOPO1 global relief model is gridded in 1 arcminute intervals, corresponding to ~1500m grid spacing at latitudes coincident with our model space.

While this spacing is suitable for larger-scale modelling, we instead incorporated seafloor bathymetry and onshore topography into our starting velocity models utilizing digital elevation models (DEMs) available via the Global Multi-Resolution Topography Synthesis (GMRT) dataset v3.9 (Ryan et al., 2009). We select the highest possible resolution of data available which is downloaded as a netCDF grid file compatible with Generic Mapping Tools (GMT), corresponding to a grid spacing of ~2 arcseconds or

roughly 50m at 40°N (Fig 5-4). For specific grid parameters, see Table A-1 in the Appendix.
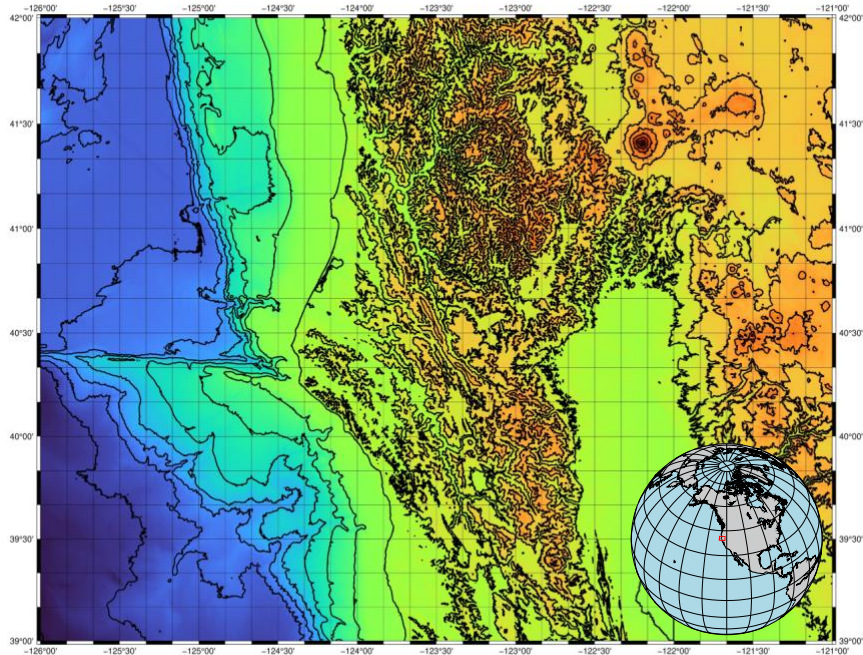


*Figure 5-4: Digital Elevation Model (DEM) of the MTJ, derived from the GMRT bathymetry and topography dataset that included in the velocity models used in Stingray for ray tracing, and ultimately, travel time inversions.*

Bathymetric and topographic data in our DEM were checked for non-physical values that may result from interpolation of multiple scattered datasets and was subsequently corrected using an average of nearest-neighbor elevations. This correction against non-physical values is vital due to the large errors and unpredictable behavior that can arise when these values are encountered during raytracing. Data processing codes are available via Github. (Ferragut, 2021).

**Velocity Models Overview**

A key element of both forward and inverse modelling in seismology is the construction and implementation of a starting velocity model with fidelity to real world structure. In the simplest case a model could be a simple 1D velocity profile. Rather than build a 3D starting velocity model exhibiting fidelity to known Earth structure from the ground up, we instead seek to utilize modelling efforts from recent seismic research in

22

Cascadia. The models we chose to explore vary greatly in scale, resolution, and fidelity, ranging from the entirety of the subduction margin down to the region immediately surrounding the MTJ. We began by identifying available reference and community velocity models specific to Cascadia. Such models are designed to be built upon and, while physically based, they reflect only large-scale structure (Stephenson et al., 2019). We also sought to use contemporary tomographic results on a regional scale that incorporate local and teleseismic earthquake data and as such can represent portions of the model space unconstrained by active-source ray coverage (Bell et al., 2016). Lastly, we aim to prepare very recent tomographic results from a small Mendocino-specific study, utilizing relocated local earthquakes, providing the most up to date information reflecting seismic structure in the region (Guo et al., 2021).

### Stephenson et al., (2019)

In 2019 the USGS released updated 3D Vp and Vs reference models (V1.6) for use in ground motion simulations and rupture modelling in the Cascadia Subduction Zone (Stephenson et al., 2019). The model includes seafloor bathymetry and is comprised of gridded nodes within discrete volumes representing geological units with differing seismic properties for continental sedimentary basins, continental crust, continental mantle, oceanic sediments, oceanic crust, and oceanic mantle. The velocity properties of these units were derived from a combination of empirical relationships and updated tomographic and geophysical results.

While the velocity model of Stephenson et al., (2019) is a useful baseline for comparison to more complex or regionally specific models, its extent is unfortunately limited to regions of Cascadia north of the Mendocino Fracture Zone (MFZ) and longitudes less than -122°00'W. This corresponds to ~40% of our target model space. The offshore southern boundary at the MFZ provides a natural break that could allow for the velocity model to be expanded by adjoining a simple oceanic lithosphere model. This is a reasonable choice for the Pacific Plate in this locale, which is much older and not internally deforming such as the Gorda Plate to the north (Chaytor et al., 2004). Expanding this model onshore is more tenuous, as the crustal thickening and transient deformation associated with triple junction passage is a target of interest and relatively

poorly constrained. Limited 2D estimations of crustal thickness from receiver functions are available (Hayes and Furlong, 2007) and could be used to adjoin a simple crustal model onshore, underlain by lithospheric mantle velocities estimated from heatflow measurements and previous tomographic results south of the MTJ (Goes et al., 1997)

**Bell et al., (2016)**

This shear-wave velocity model is the result of a margin-wide Rayleigh wave tomography study using teleseismic OBS data from years 1-3 of the Cascadia Initiative (Toomey et al., 2014). The full model includes Vp, Vs, and density. It spans 36° to 54° in latitude and -136° to -118° in longitude and model is regularly sampled at a spacing of 0.2° in both dimensions. This covers the entire Cascadian Subduction Zone, extending further south than the Stephenson et al., (2019) model and beyond the MFZ. As opposed to the gridded velocity model described above, this model is layered vertically. A 94x94 element nodal grid (8281 nodes) defines the locations of each 1D velocity depth profile. Bathymetry from the ETOPO1 global relief model (Ryan et al., 2009) is included in the model but is flattened in onshore regions and zeroed in elevation at sea-level. Bell et al. divide the crust into 3 distinct regions: oceanic crust, forearc, and continental crust. Onshore structure is relatively simple, but oceanic and forearc crust are divided into layers comprising of water, marine sediments (Divins, 2003), and igneous basement rock, with the igneous layer further subdivided into multiple layers

While the starting models in this study are prepared with structural detail and incorporate a greater degree of complexity than the models of Stephenson et al., (2019), we use the final model from their tomographic inversion. The active-source data we prepare here is restricted in its ability to resolve depths much further than upper lithospheric mantle where mantle-refracted *Pn* waves may yield constraints on seismic velocities. By contrast, the Rayleigh waves used in Bell et al., (2016) are, in general, more sensitive to velocity variations at depths beyond 15 – 20km due to the period-dependent sensitivity of surface waves and the limited use of short period data due to issues with multipathing (Bell et al., 2016). The Rayleigh wave results provide data-based velocity structure constraints at depth, while the crustal and near-surface velocity structure is largely the same as the high-fidelity starting model. This makes the Bell et al.

model a useful one for raytracing and eventually inverting legacy active-source data within the context of future multiscale tomography applications.

### Guo et al., (2021)

In March 2021, new tomographic results investigating fluids at the plate interface were published in a small regional study centered on the MTJ (Guo et al., 2021). Like Bell et al., (2016), this velocity model is the result of OBS data from the Cascadia Initiative (Toomey et al., 2014) and uses recordings from years 2-4, as well as data catalogued by the Northern California Earthquake Datacenter (NCEDC). Model bounds very nearly coincide with our own model space and range from ~ 39° to ~42° latitude and -126° to -121° in longitude. Vp and Vs values are represented on a variably spaced nodal grid with refined grid-spacing corresponding to regions of higher station and event density. The finest grid-spacing occurs in Z and ranges from 3 to 5 km, increasing with depth. Horizontally grid-spacing ranges from 5 to 20 km. Elevation is considered, albeit only coarsely given the 3km spacing in Z, and zeroed at sea level with negative values corresponding to bathymetry and positive values (peaking at a flat 1.5km elevation) corresponding to onshore topography.

Unlike Bell et al., the dataset used in this study is comprised of local earthquakes occurring at, or very near, the Mendocino Triple Junction. As with the Bell et al. model, Guo et al. provide a velocity model utilizing data of only one "scale". Being constrained by only local earthquake data provides a useful companion in comparing modelling via other general large-scale models (Stephenson et al., 2019) or models derived from data sensitive to other elements of Earth structure (Bell et al., 2016).

### Velocity Model Processing
### Stephenson et al., (2019)

The original velocity of Stephenson et al., 2019 provided by the USGS covers a massive area spanning the entirety of the Cascadia Subduction Zone. For our purposes, only a small subset of this velocity model, in its entirety consisting of >300,000,000 lines of text, was to be implemented as a starting model for ray tracing. To reduce memory and computational requirements, this model was first iterated over and subset to the

approximate bounds of our region of interest. The model provides both P and S wave velocity values varying in 3D and once subset is easily repurposed by resampling and interpolation. A simple 1D interpolation scheme is applied to vertical (varying in Z) columns in the model space, followed by plane interpolation in 2D at successive depth slices. The resultant grid spacing and model dimensions are used to construct an instance of srModel.

## Bell et al., (2016)

Velocity data was available in a formatted text file via the publisher and provides layer thickness, Vp, Vs, and lithologic densities that may be used to convert between compressional and shear wave velocities after the methods of Brocher (2005). Unlike the purely gridded models, this layered velocity model consists of 1D velocity profiles at each point in space rather than a list of coordinates in 3D, with associated seismic velocities and material properties. The number of layers in each velocity profile is variable, as is the thickness of the layers within. The data file consists of a file header specifying model parameters (N nodes, data order, etc.) followed by a consecutive list of 1D profiles located on a 2D grid. Each 1D profile has an individual header preceding the data describing the number of layers and geodetic coordinates of the profile.

The model is parsed using these headers as a guide to populate a masked 3D array, allowing for a variable array length in the Z dimension and only passing values within our queried model space. To convert from layers to a nodal grid, individual 1D profiles are resampled at layer midpoints and boundaries. These are then interpolated to constant spacing in Z to produce a 3D grid of uniform depth. Subsequently, model layers resampled using a 2D interpolation scheme.

Nodes with Vp values less than or equal to 1.5 km/s (an approximate sounding velocity) are masked as water. Columns containing water are iterated over, retaining only nodes with velocities values indicative of sediments, or faster, and then sheared vertical to flatten on bathymetry. Onshore velocity profiles are then truncated and sheared vertically to produce a uniformly flattened velocity model that is subsequently hung from an elevation profile during modelling.

## Guo et al., (2021)

The approach to parsing and resampling the velocity model of Guo et al., is very similar to that used in processing the model of Bell et al., albeit simpler due to the lack of velocity layering. The velocity model is stored as a row-major (longitude major) list of coordinate-value pairs that can be simply iterated over and read into a 3D array using the corresponding indexing. This can then be interpolated vertically at each column, and subsequently interpolated across planes of constant depth to refine grid spacing. With water and bathymetry coarsely represented it is particularly important that nodes with Vp values of 1.5 km/s or slower are masked first to prevent interpolation from bleeding anomalously slow velocities into the near surface of the model.

After the grid spacing of the model is refined water is stripped out of the model in the same fashion as with the Bell et al. model. Nodes with velocities indicative of water are trimmed from model columns and these columns are then sheared vertically to produce a model flattened on the surface. This model is then hung from a higher resolution elevation model during loading in Stingray.

# CHAPTER VI: DATA STRUCTURES & WORKFLOW

The legacy active-source dataset compiled here is converted into data structures compatible with a fully 3D ray tracing and traveltime inversion routine (Toomey et al., 1994) implemented through a MATLAB software package consisting of the programs Stingray (forward problem) and TomoLab (inverse problem). Data visualization and traveltime picking of active-source data is facilitated by a third associated package tlPicker. Below (Fig. 6-1) is an overview of directory structure and the data structures used.
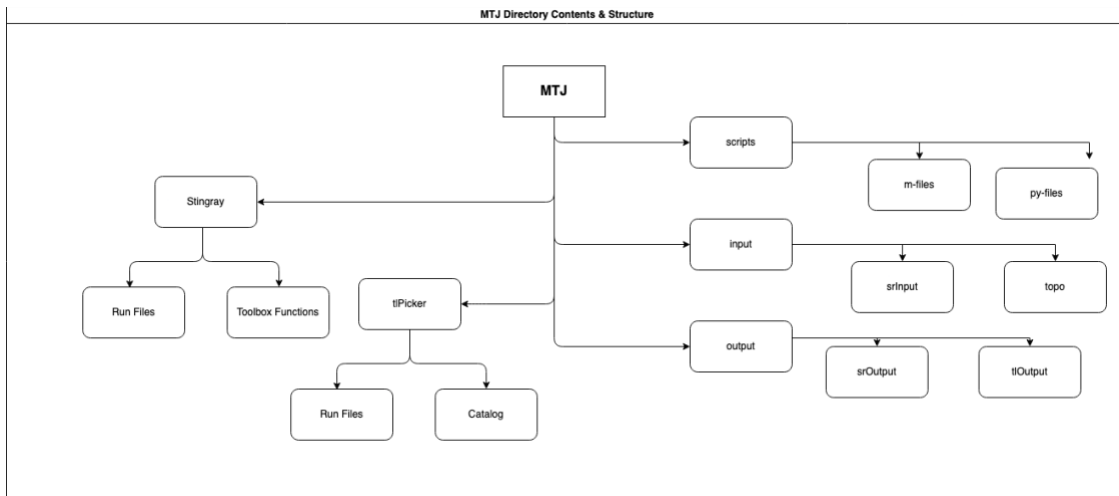


*Figure 6-1: Directory structure used in the Stingray and tlPicker workflow and that of the associated code repository. This working directory is synced to an HPC to perform the calculations necessary for forward and inverse modelling.*

## Stingray Data Structures

### srGeometry

The data structure srGeometry defines the experimental geometry and coordinate system for the forward and inverse problems in Stingray/TomoLab. While calculations are performed on a Cartesian grid, srGeometry can be defined in either geodetic coordinates or Universal Transverse Mercator (UTM). Many of the legacy experiments described above utilize the UTM coordinate system, but both geodetic and UTM options are provided here for some models and are denoted by a relevant filename suffix. Additionally, different srGeometry files exist that correspond to the velocity models discussed above that have been converted to srModel.

| Filename | Ref. System | Model | Bounds |
|----------|-------------|-------|--------|
| srGeometry-Steph | Geodetic/UTM | Stephenson et al., (2019) | [-125.8, -121.4, 40.0, 42.0] |
| srGeometry-Bell | Geodetic/UTM | Bell et al., (2016) | [-125.8, -121.4, 39.2, 41.6] |
| srGeometry-Guo | Geodetic | Guo et al., (2021) | [-125.8, -121.4,  39.2, 41.6] |

*Table 6-1: Geometry files for different velocity models usable for forward and inverse modelling.*

### srElevation

We use the most recent GMRT elevation model to build srElevation, the data structure that houses bathymetry and topography in Stingray. srElevation is a structure in loading velocity models in Stingray, and bounds are set slightly larger than those of the available models. When srModel is instantiated at loading, srElevation is read in, overlaid on the model, and subsequently interpolated to model bounds. A single srElevation file exists and can be used for any of the models, being converted to the appropriate coordinate system during srModel creation.

### srModel

The velocity models here are parsed and process as outline above into MATLAB compatible data files to facilitate computational efficiency. The parsed and resampled model matrices are then used to construct srModel. The srModel data structure consists of two fields: (1) A grid header describing nodal dimensions (nx, ny, nz), spacing (gx, gy, gz), and origin of the coordinate reference frame, and (2) Data fields containing the inverse of seismic velocities (slowness), to facilitate use in the ray tracing and tomographic algorithms of Stingray.

| srModel Grid Parameters | | | |
|----------|-------------|-------|--------|
|  | srModel-Steph | srModel-Bell | srModel-Guo |
| srModel.nx | 667 | 2199 | 2200 |
| srModel.ny | 374 | 1199 | 1200 |
| srModel.nz | 121 | 225 | 225 |
| srModel.gx | 500m | ~ 200m | 200m |
| srModel.gy | 500m | 200m | 200m |
| srModel.gz | 500m | 200m | 200m |

*Table 6-2: Header values for different velocity models describing velocity grid dimensions and spacing and housed in the data structure srModel.*

### srStation

The location and elevation information for receivers from each phase of the MTJSE and the nearby onshore/offshore experiment at Cape Blanco are stored in

srStation files. Receivers are aggregated into different srStation files based on geometry, source type, or data gather. Onshore seismographs and offshore OBS/OBH stations. For example, a 2D wide-angle line like WA1 may be a single srStation file for the '93 MENI onshore shots. Alternatively, the reoccupied WA1 from '94 MENII that recorded both targeted 2D wide-angle profiles as well as airgun shots in a fan geometry could be represented both as a single srStation file for the 2D profile, and as a component of a larger srStation file containing all '94 receiver lines. Filenames are written descriptively with appropriate line names or experiment phases.

| srStation Examples | |
|---|---|
| **Filename** | **Stations** |
| srStation_MENI_Line1 | 573 |
| srStation_MENII_WA1 | 128 |
| srStation_MENA | 24 |

*Table 6-3: Examples of srStation file naming convention and associated number of stations*

### srEvent

Stingray uses srEvent to house location and elevation or depth information for energy sources in the model space. srEvent can be specified with different source types such as airgun shots, borehole explosions, local earthquakes, and teleseismic earthquakes. The majority of sources recorded in this dataset came from offshore shots from the R/V *Ewing*'s airgun array during the MENDO phase of the MTJSE. Shots were ascribed different line names and ID values corresponding to geometry or the intended onshore receivers.

The onshore 3D array, referred to here as MENA, recorded the entirety of the airgun shots and is a reliable source of shot locations. Header information was extracted from all SEG-Y data files available for the array stations and cross referenced to check for consistency. Each file has 35850 shot IDs in agreement with PASSCAL Data Report 96-008 for the MENA dataset. Some of these shot IDs are erroneously duplicated, however. Event metadata searched iteratively for unique shot ID field and cross referenced again for consistency across stations. Duplicated shot IDs were removed with the first unique ID encountered being retained. This resulted in 35,765 unique events. These unique event IDs were then later confirmed to match those utilized in the results of

Hole (2000), which also differed from the content of the data report. For shot ID ranges by line refer Table 5-8 in the previous chapter.

Shot location data was also pulled directly from SEG-Y headers, with duplicate fields being eliminated. Coordinates were archived referenced to UTM Zone 10 and were similarly cross-referenced across stations for consistency. We retain UTM coordinates for airgun shots, but also use PyProj to convert to geodetic coordinates, creating srEvent structures for each coordinate system. To facilitate modelling flexibility, the complete airgun srEvent files are also split into individual lines, each labeled with a suffix of the relevant shot line. This allows ray tracing or inversion of specific experiment deployments or receiver lines.

| srEvent Examples | |
| --- | --- |
| Filename | Shots |
| srEvent_MENI-Line1 | 8 |
| srEvent_MENI-Line6 | 8 |
| srEvent_MENI-Line9 | 11 |
| srEvent_MCKSH | 4 |

*Table 6-4: Examples of srEvent file naming convention and associated number of shots, here borehole explosions.*

Onshore sources consist of borehole explosives at varying depths and locations along 2D receiver lines. Metadata from these shot locations are extracted from SEG-Y data for the MENI and MCKSH experiments and used to create srEvent structures. Each srEvent file corresponds to an individual line.

### tlPicker Data Structures

The data visualization platform used to display record sections, predicted travel times, and to make traveltime picks. The functions of tlPicker provide IO capabilities for SEG-Y data based on a user constructed data structure mapping byte-location specific header and trace data to accompanying Stingray structures. To view SEG-Y data, one must first use helper scripts to construct the segyCatalog object.

### segyCatalog

This data structure serves as a road map for querying the actual seismic trace data when plotting and picking. The tlPicker package provides helper scripts that use specified

srEvent and srStation structures to attempt to iterate over a directory of SEG-Y files and build a mapping between byte locations in data files and the Stingray structures. To do this, tlPicker utilizes a custom SEG-Y I/O function *read_segy*. When dealing with SEG-Y data of uncertain origin or non-standard formatting, one must take care with assumptions made in *read_segy*. In our case, the data from the MENA portion of the MTJSE was largely complete, but some non-standard SEG-Y header values existed, such as scalars applied to coordinates. Therefore, to have these files read correctly requires a degree of customization when reading in specific byte locations. For example, the trace headers for the MENA data have an incorrect value of [-10] (a SEG-Y shorthand for dividing UTM coordinates by a factor of 10) written at byte location 71. If *read_segy* was not adjusted for this UTM coordinates in the experiment, and all calculations derived from them, would be unreliable. This is unfortunately the case with many of these SEG-Y flies. For specifics on trace header values and byte location mapping, see Table A-3 and further documentation in the code repository on Github (Ferragut, 2021).

## tlPick

Travel time picks are read into tlPicker and used in the forward and inverse problem calculations of Stingray through the data structure tlPick and stored as an ASCII file. Picks may be made interactively in tlPicker and saved in this format or alternatively existing picks could be converted to this format. Each tlPick file corresponds to a particular seismic phase and multiple may be plotted concurrently. Each line in the tlPick file consists of fourteen fields. These include identifying information, such as station, channel, eventid, and phase information, followed by relevant data information, i.e., pick time, assigned uncertainty in milliseconds (ms), filter limits and order, and amplitude scaling. Lastly, several fields contain user information such as name, time when picked, and additional comments.

## Workflow for Stingray & tlPicker

### Forward Modelling

The bulk of traveltime picks in our dataset correspond to arrivals at receivers in the 3D onshore array originating from the ~36,000 offshore airgun shots. To explore data

and model fit, we focus forward modelling on this array to compare predicted and observed (picked) arrivals. Stingray is used to ray trace through the Bell et al., (2016) Vp model and predict first arrival times for all source/receiver combinations in the 3D array (srStation-MENA) and offshore shot data structures (srEvent-MENDO). These predictions are plotted on record sections and compared to both data and observed travel time picks from Hole (2000)

## High Performance Computing (HPC)

Due to the large computational requirements, both in memory and processing power, we utilize the University of Oregon high-performance computer, Talapas. The working directory is synced from a local workstation to the HPC, and execution of the code is handled via the Slurm Workload Manager. The large number of model nodes and rays being traced in 3D necessitates a substantial availability of memory. To run these calculations, we therefore use the 12 cores (the maximum) on a 1TB RAM large memory node of Talapas and run the Stingray code in parallel. Memory usage for tracing airgun shot to 3D array stations, for example, typically uses ~400gb of RAM. To ray trace the entirety of the experiment concurrently may require increasing available memory to the highest tier, the 4TB large memory node.

## Using Existing Picks

Picks may be made in tlPicker, or existing picks can be converted to a compatible form. In this case, we are utilizing travel time picks from different sources and of different formats. To make these measurements useable, we iteratively read in pick files and extract fields containing source information, picked time, and error. Optionally, a velocity reduction correction may be applied. For example, the arrivals used in the work of Hole (2000) are picked at a reduction velocity of 6 km/s. Source and receiver geometry is then used to calculate a correction which is applied to the picked time.

With the relevant information extracted, these fields are then arranged using a format string matching that of the tlPick file convention. The tlPick file can then be

loaded into tlPicker and plotted over data to assess pick quality and model misfit (Fig. 6-3).
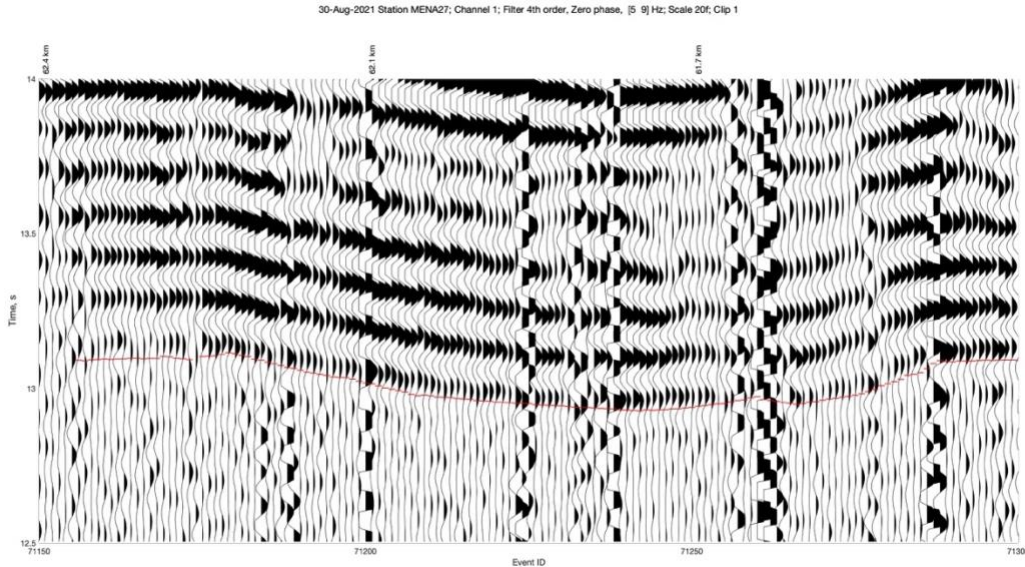


*Figure 6-2: Travel time picks from Hole (2000), converted into the tlPick file format and plotted in tlPicker. The upper X-axis shows source/receiver offset.*

Customizable shell scripts to perform this process for other travel time picks that may be acquired in the future are available via Github (Ferragut, 2021). For specifics of string formatting see the Appendix and associated code repository.

**Predicting Travel Times**

To predict travel times and plot them (Fig. 6-3), an empty tlArrival structure is created that is large enough to house all station and source combinations. When performing inversions, this tlArrival structure will contain seismic arrival information that is adjusted throughout several iterations and models. By starting with an empty tlArrival structure and only performing a single iteration of the forward problem, we get an output structure that houses travel times between sources and stations that have been ray traced through our starting model.
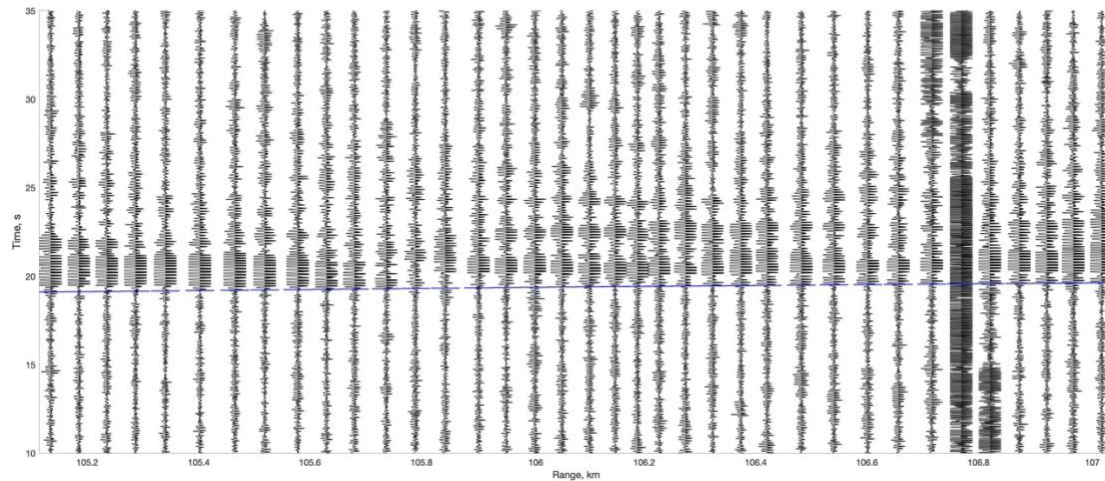
*Figure 6-3: Predicted arrivals(blue) for a station in the onshore 3D array of the MTJSE. As is evident, this station (MENA4) exhibits very little misfit between predicted travel times and the actual onset of the P-wave energy. The upper X-axis shows airgun shot ID.*

When a forward modelling run has been completed, several output folders are generated by Stingray/TomoLab and labeled with a unique run ID. The output folder from the desired run is then passed as an argument to the Stingray toolbox function *tlOutput2tlPick.m*, which converts the calculated travel times into tlPick structures. An experiment-specific helper script of the form *get_####_predictions.m* (for example *get_MENA_predictions.*m) provides a workflow to read in modelling outputs and generate these synthetic travel time pick files. Once generated, they may be loaded into tlPicker like any other tlPick file and plotted on a record section as predicted arrival times for a particular model and source/receiver combination (Fig. 6-4).

**Prediction Error & Residuals**

Comparing the predicted arrival times and picked arrivals can provide insight into how well a model captures real velocity structure. This can be achieved qualitatively by plotting record sections and overlaying arrival times or more quantitatively by calculating the residual times, i.e., the difference between predicted and picked arrival times.
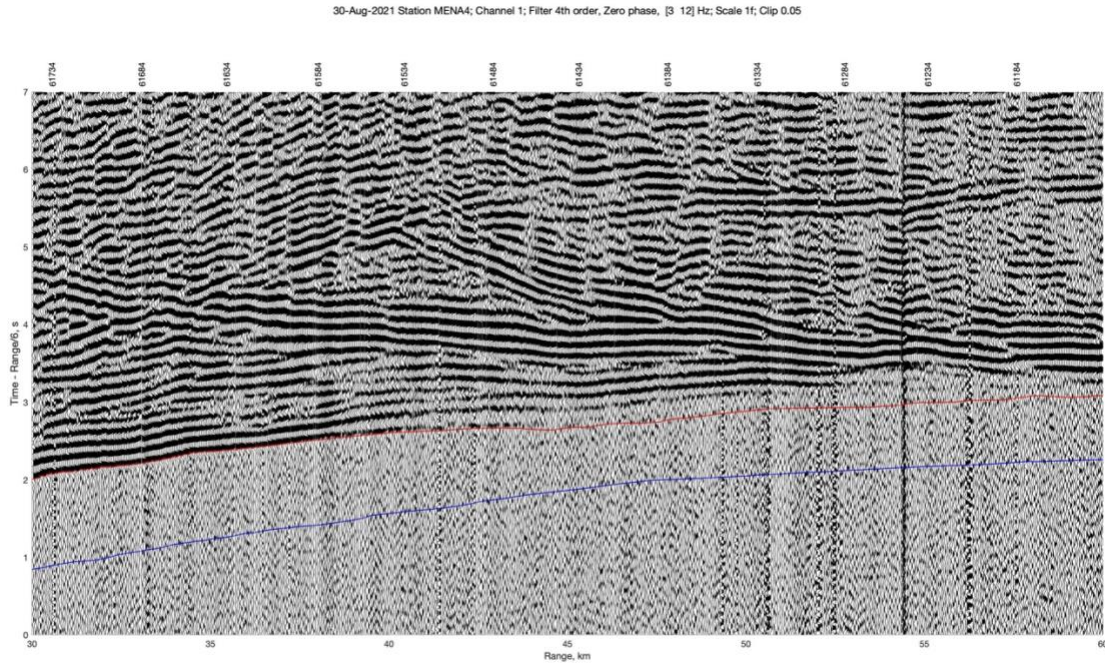
*Figure 6-4: Graphical comparison of predicted arrival times (blue) and picked arrival times (red) at MENA4 showing predictions consistently 1s early. The upper X-axis shows airgun shot ID.*

Misfit between predictions and observations (picks) varies greatly, from 10s of milliseconds to multiple seconds (Fig 6-4; Fig 6-5). Even in high-misfit source/receiver combinations where predictions and picks may lag by > 1 second, predicted arrivals are conformal to the overall trends of actual arrivals, indicating that the bulk of velocity structure is moderately well-represented in the Bell et al. model. Static offsets may be the result of undetermined near surface structure at receivers and/or beneath airgun shots.

For all station/receiver combinations travel times are predicted during forward modelling. Only a subset of these predictions corresponds to seismograms that have been picked. Residuals are calculated by subtracting observed arrival times from predicted arrival times derived from ray tracing. In 6-6 misfits have been averaged by station locations, that is, every available misfit calculation spanning all airgun shots is averaged. The results seem to show systematically early predictions below the triple junction itself, with lower misfit to the north where the Gorda slab exists. Similarly, Fig. 6-7 shows misfit between predicted and observed arrivals times is averaged by airgun shot, i.e., for a single shot, all misfits associated with that shot ID are averaged to explore the contributions from potential variations in seafloor structure.

36
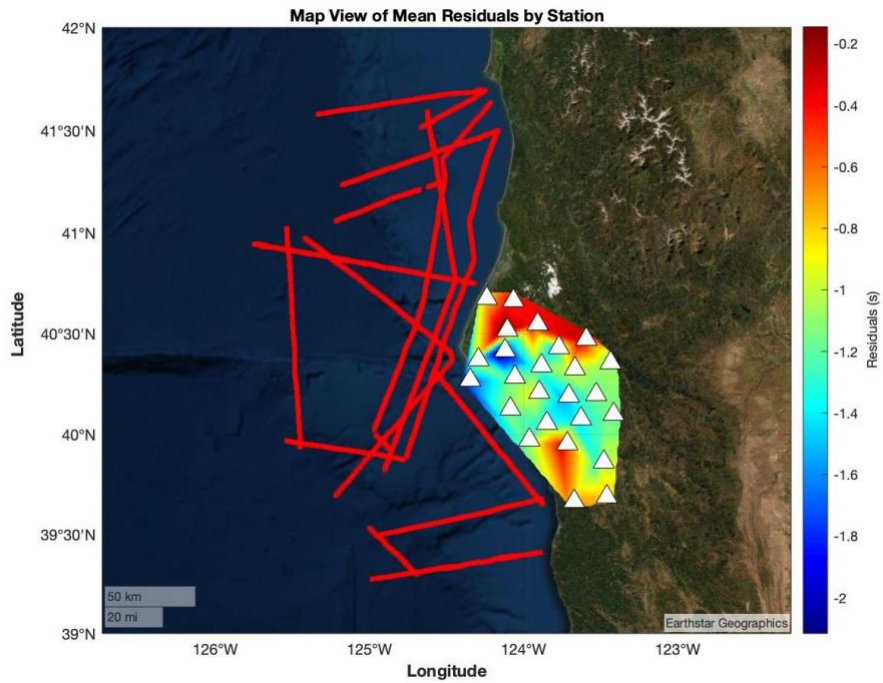
*Figure 6-5: Map of shot lines (red) and the onshore 3D array (MENA, white triangles) with travel time misfit averaged station by station. Variations may indicate near surface structure not present in the velocity model*
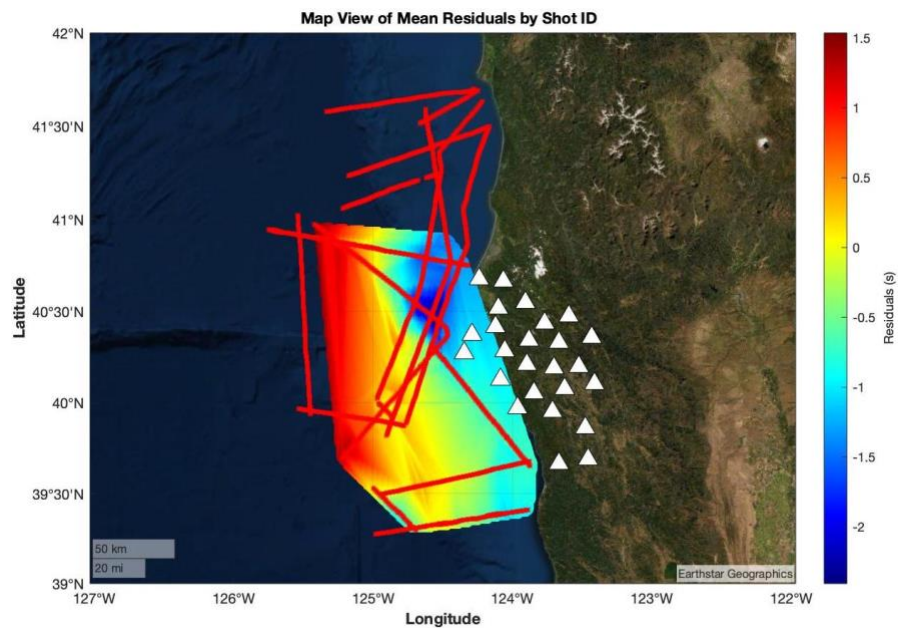


*Figure 6-6: Map of shot lines (red) and the onshore 3D array (MENA, white triangles) with travel time misfit averaged at each shot location.*

As airgun shots get further from the onshore array, predicted arrivals tend to lag picked arrivals without much variation. A small region of shots does coincide with earlier than expected predictions, however. These shots are also adjacent to the region in the station averaged map displaying generally early predictions. Given the large misfit and spatial variations, it is safe to say that the current velocity model, Bell et al., (2016), does not adequately capture the structure at the MTJ. Improvements to these models may be made by initially utilizing all active-source data jointly, and in the future, performing fully multi-scale tomographic inversion.

# CHAPTER VII:    CONCLUSION

The Mendocino Triple Junction connects the Cascadia Subduction Zone and the San Andreas Fault to the south. It migrates northward as the Gorda Plate subducts beneath North America, resulting in a complex pattern of crustal deformation and the formation of a slab gap and the San Andreas Fault in its wake. Despite its high level of seismic activity and importance in potential earthquake hazards, our knowledge of its control on the Cascadia Subduction Zone and the geologic variables governing its evolution remain limited in resolution. To image the subsurface structure of the MTJ at high-resolution and in 3D requires simultaneous utilization of multiple scales of seismic data. We have synthesized a self-consistent dataset of all available legacy active-source data at the MTJ and structured it to be compatible with a modern 3D tomography routine capable of jointly inverting local earthquake data, teleseismic earthquake data, and active-source data. Using tomographic results from the region we explore misfit between forward modelled arrival times and picked arrival times obtained from previous active-source work in the region. The resulting high degree of misfit indicates further improvements can be made in seismic imaging at the MTJ and encourages the future pursuit of 3D multi-scale seismic tomography in southern Cascadia.

# APPENDIX

**GMRT DEM Grid File Information**

| Projection: | Cylindrical Equidistant |
|---|---|
| Format: | GMT netCDF (32 bit float) |
| Maximum Elevation: | 4299.98730469 m |
| Minimum Elevation: | -4020.93212891 m |
| Longitude Bounds: | -126.00000000°, -120.999572754° |
| Latitude Bounds: | 38.9999758356°, 42.0003251483° |
| Spacing in X: | 0.000549376757426° |
| Spacing in Y: | 0.000417643278502° |
| # Nodes in X: | 9103 |
| # Nodes in Y: | 7185 |
| Total # Nodes: | 18206 |

*Table A-1: Grid file parameters for the GMRT digital elevation model (DEM) used in creating srElevation, which may be accessed through the Generic Mapping Tools (GMT) package command "grdinfo"*

**String Formatting in tlPicker**

To convert picks used in other software or picks simply stored coordinate-value paired text-based files, shell scripts are provided in the Github repository (Ferragut, 2021). These simply read in text files line by line, using *awk* fields to extract the required information. These fields can easily be adjusted to accommodate other string formats by switching the queried location in the input string.

| **String Format: Derived from "save_tlPick.m" in tlPicker** | |
|---|---|
| Fields | "station", "channel", "eventid", "phase", "time", "unc", "filtLim0", "filtLim1", "filtOrder", "filtZeroPhase", "scale", "user", "lddate", "UNUSED", "comment" |
| Format String | "%6s%2i%8i%8s%10.4f%7.4f%5.1f%5.1f%2i%2i%10.2e%10s%17.5f%2i%38s%-80s\n" |

*Table A-2: Format string to specify appropriate spacing and fields for a tlPick file. See shell script reformat_picks_MTJ.bash in the associated Github repository (Ferragut, 2021) for specifics on conversion to the tlPick format. Note that "UNUSED" field as labeled in the tlPicker documentation corresponds to two sub fields formatted as %2i%38s.*
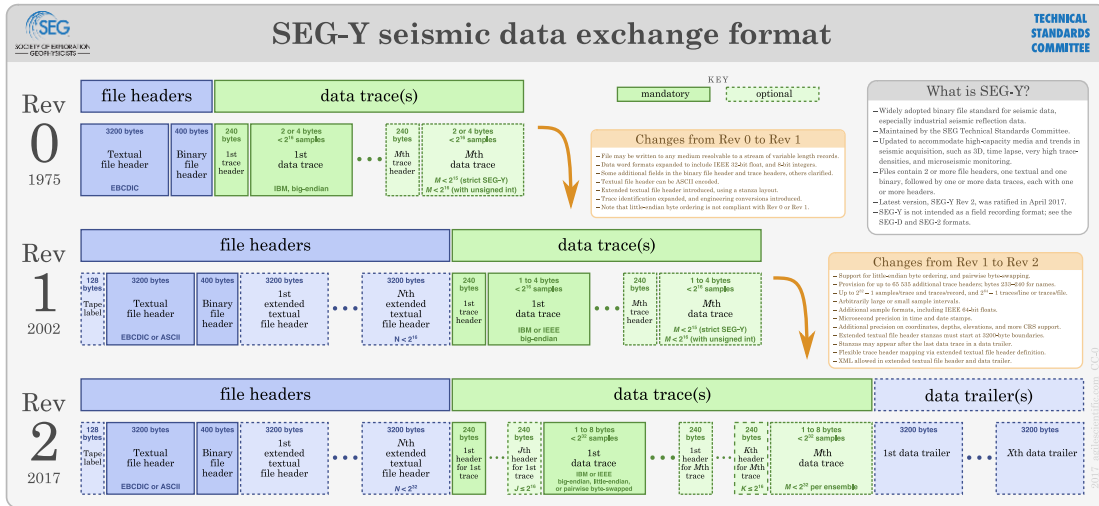
# SEG-Y Revision History



*Figure A-1: Summary of revisions and changes to the Society of Exploration Geophysicists seismic data standard format SEG-Y. Accessed from https://wiki.seg.org/wiki/SEG-Y*

# SEG-Y Byte Locations Mapping Example – MENII

| | byte_loc | ... | max |
|---|---|---|---|
| TRACE_SEQUENCE_LINE | 1 | ... | 3.100000e+01 |
| TRACE_SEQUENCE_FILE | 5 | ... | 3.100000e+01 |
| FieldRecord | 9 | ... | 1.300000e+02 |
| TraceNumber | 13 | ... | 1.000000e+00 |
| EnergySourcePoint | 17 | ... | 1.300000e+02 |
| CDP | 21 | ... | 1.398000e+03 |
| CDP_TRACE | 25 | ... | 3.100000e+01 |
| TraceIdentificationCode | 29 | ... | 1.000000e+00 |
| NSummedTraces | 31 | ... | 0.000000e+00 |
| NStackedTraces | 33 | ... | 0.000000e+00 |
| DataUse | 35 | ... | 0.000000e+00 |
| offset | 37 | ... | 2.780820e+05 |
| ReceiverGroupElevation | 41 | ... | 2.670000e+06 |
| SourceSurfaceElevation | 45 | ... | -7.500000e+04 |
| SourceDepth | 49 | ... | 0.000000e+00 |
| ReceiverDatumElevation | 53 | ... | 0.000000e+00 |
| SourceDatumElevation | 57 | ... | 0.000000e+00 |
| SourceWaterDepth | 61 | ... | 0.000000e+00 |
| GroupWaterDepth | 65 | ... | 0.000000e+00 |
| ElevationScalar | 69 | ... | -1.000000e+04 |
| SourceGroupScalar | 71 | ... | 1.000000e+00 |
| SourceX | 73 | ... | 2.695590e+05 |
| SourceY | 77 | ... | 4.536384e+06 |
| GroupX | 81 | ... | 5.407390e+05 |
| GroupY | 85 | ... | 4.481886e+06 |
| CoordinateUnits | 89 | ... | 0.000000e+00 |
| WeatheringVelocity | 91 | ... | 0.000000e+00 |
| SubWeatheringVelocity | 93 | ... | 0.000000e+00 |
| SourceUpholeTime | 95 | ... | 0.000000e+00 |
| GroupUpholeTime | 97 | ... | 0.000000e+00 |
| SourceStaticCorrection | 99 | ... | 0.000000e+00 |
| GroupStaticCorrection | 101 | ... | 0.000000e+00 |
| TotalStaticApplied | 103 | ... | 0.000000e+00 |
| LagTimeA | 105 | ... | 0.000000e+00 |
| LagTimeB | 107 | ... | 0.000000e+00 |
| DelayRecordingTime | 109 | ... | 0.000000e+00 |
| MuteTimeStart | 111 | ... | 0.000000e+00 |
| MuteTimeEND | 113 | ... | 0.000000e+00 |
| TRACE_SAMPLE_COUNT | 115 | ... | 7.500000e+03 |
| TRACE_SAMPLE_INTERVAL | 117 | ... | 8.000000e+03 |
| GainType | 119 | ... | 1.000000e+00 |
| InstrumentGainConstant | 121 | ... | 3.200000e+01 |
| InstrumentInitialGain | 123 | ... | 0.000000e+00 |
| Correlated | 125 | ... | 0.000000e+00 |
| SweepFrequencyStart | 127 | ... | 0.000000e+00 |
| SweepFrequencyEnd | 129 | ... | 0.000000e+00 |
| SweepLength | 131 | ... | 0.000000e+00 |
| SweepType | 133 | ... | 0.000000e+00 |
| SweepTraceTaperLengthStart | 135 | ... | 0.000000e+00 |
| SweepTraceTaperLengthEnd | 137 | ... | 0.000000e+00 |
| TaperType | 139 | ... | 0.000000e+00 |
| AliasFilterFrequency | 141 | ... | 0.000000e+00 |
| AliasFilterSlope | 143 | ... | 0.000000e+00 |
| NotchFilterFrequency | 145 | ... | 0.000000e+00 |
| NotchFilterSlope | 147 | ... | 0.000000e+00 |
| LowCutFrequency | 149 | ... | 0.000000e+00 |
| HighCutFrequency | 151 | ... | 0.000000e+00 |
| LowCutSlope | 153 | ... | 0.000000e+00 |
| HighCutSlope | 155 | ... | 0.000000e+00 |
| YearDataRecorded | 157 | ... | 1.994000e+03 |
| DayOfYear | 159 | ... | 1.720000e+02 |
| HourOfDay | 161 | ... | 2.300000e+01 |
| MinuteOfHour | 163 | ... | 4.900000e+01 |
| SecondOfMinute | 165 | ... | 5.800000e+01 |
| TimeBaseCode | 167 | ... | 2.000000e+00 |
| TraceWeightingFactor | 169 | ... | 0.000000e+00 |
| GeophoneGroupNumberRoll1 | 171 | ... | 0.000000e+00 |
| GeophoneGroupNumberFirstTraceOrigField | 173 | ... | -3.576000e+03 |
| GeophoneGroupNumberLastTraceOrigField | 175 | ... | 0.000000e+00 |
| GapSize | 177 | ... | 0.000000e+00 |
| OverTravel | 179 | ... | 0.000000e+00 |
| CDP_X | 181 | ... | 8.088536e+08 |
| CDP_Y | 185 | ... | 1.627412e+09 |
| INLINE_3D | 189 | ... | 1.263423e+09 |
| CROSSLINE_3D | 193 | ... | 1.308640e+09 |
| ShotPoint | 197 | ... | 1.627390e+09 |
| ShotPointScalar | 201 | ... | 0.000000e+00 |
| TraceValueMeasurementUnit | 203 | ... | 8.000000e+03 |
| TransductionConstantMantissa | 205 | ... | 6.650900e+04 |
| TransductionConstantPower | 209 | ... | 1.994000e+03 |
| TransductionUnit | 211 | ... | 1.720000e+02 |
| TraceIdentifier | 213 | ... | 2.300000e+01 |
| ScalarTraceHeader | 215 | ... | 4.900000e+01 |

*Table A-3: Byte locations of SEG-Y trace header components as read in via SEGYSAK.*

## Experiment Geometry and SEG-Y Files

Even when following a file naming convention, it may not always be clear what each SEG-Y file may represent, particularly when these conventions and data gathering procedures vary by individual experiment. This is the case with the archived datasets collated here. Reading each data file by hand can be time consuming and occasionally difficult, but a useful overview is to reference maps of experiment geometry present in the trace headers. Below is an example of a map showing how the data was cut and gathered, showing locations for both sources and receivers, highlighting what the content of the SEG-Y file in question is. Further maps may be generated using the helper scripts in the code package.



*Figure A-2: Example of the extraction and plotting of shot / receiver geometry on a file-by-file basis*

## Shot Gather Record Section Examples

The MTJ code repository has a number of helper scripts to aid in reading, writing, and plotting SEG-Y data. The Python packages ObsPy and SEGYSAK are particularly useful for this. Below are output of *create_record_section_MENI*.py and show the reportedly clearest shots on each line for the onshore MENI experiment.
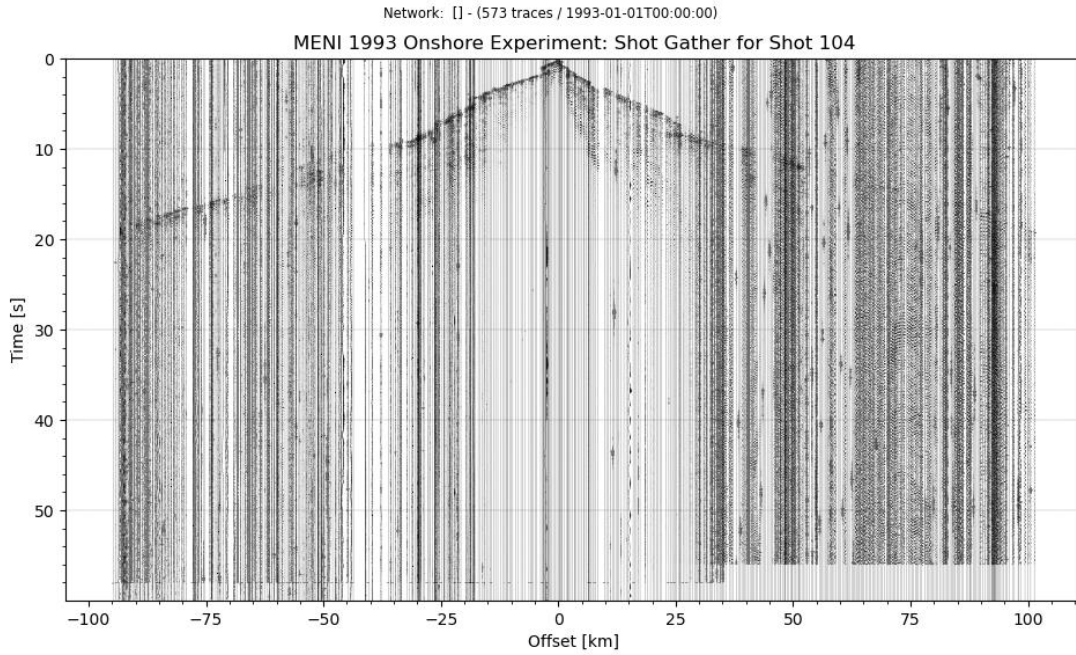
*Figure A-3: Example of record section plotting with ObsPy for shot gather on Line 1 in the onshore phase of the MTJSE*
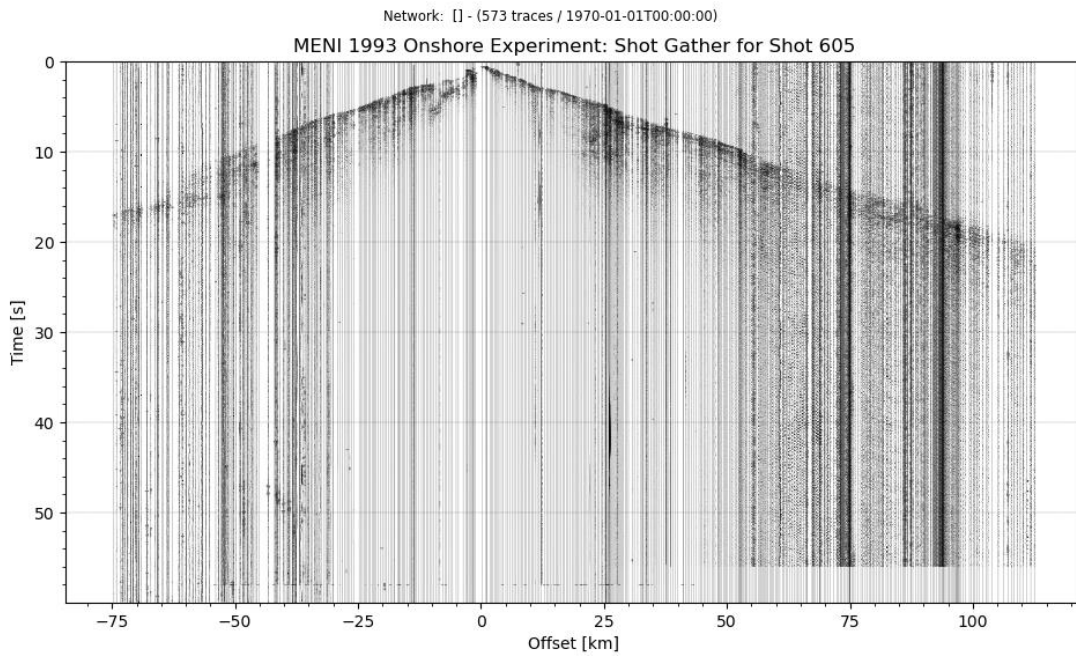


*Figure A-4: Example of record section plotting with ObsPy for shot gather on Line 6 in the onshore phase of the MTJSE*
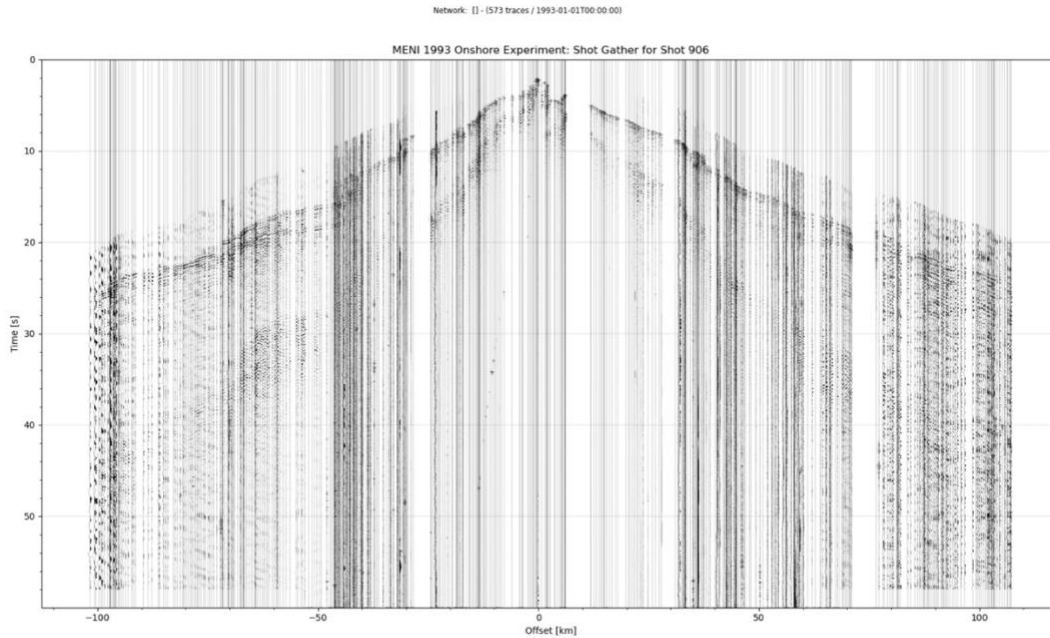
*Figure A-5: Example of record section plotting with ObsPy for shot gather on Line 9 in the onshore phase of the MTJSE*

## Velocity Model Supplementary Details

## Bell et al., 2016

As perhaps the most useful starting model provided, additional details of the Bell velocity model are shown below, as published in Bell et al., (2016).  Both water and sedimentary layers are derived from relatively course global models.

| Model layer | Thickness (km) | r (g/cm$^3$) | VP (km/s) | VS (km/s) |
|---|---|---|---|---|
| Water | ETOPO1 | 1.030 | 1.500 | 0.000 |
| Sediment | NOAA model | 2.000 | variable | variable |
| Layer 2A | 0.4 | 2.450 | variable | variable |
| Layer 2B | 1.5 | 2.450 | 5.000 | 2.630 |
| Layer 3 | 5.0 | 3.050 | 6.800 | 3.890 |

*Table A-4: Starting velocity model details, Bell et al., (2016)*

# USGS Sediment Thicknesses



*Figure A-6: A higher resolution sediment thickness map produced by the USGS that could be added to models for better fidelity.*

## Legacy Experiment Compilation

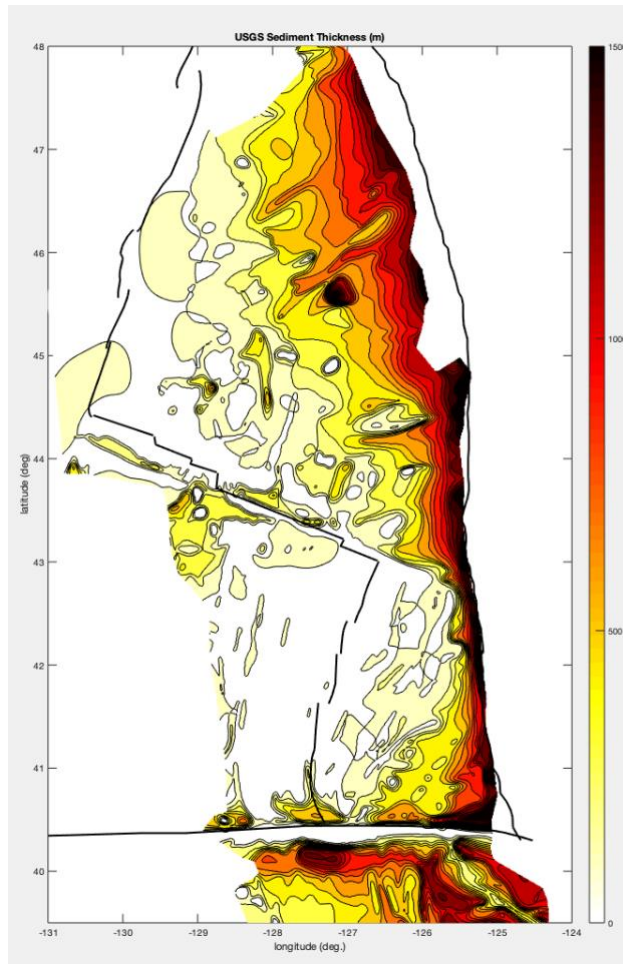| Year | Location | Reference for Data | Reference for Interpretation | No. Shots | No. Receivers | No. Raypaths |
|---|---|---|---|---|---|---|
| 1960 | Vancouver Island, British Columbia | White and Savage, 1965 | White and Savage, 1965 | 98 | 30 | 2940 |
| 1965 | Oregon and Washington shot | Berg et al., 1966 | Berg et al., 1966 | 1 | 10 | 10 |
| 1965 | Oregon and California margin, two-ship refraction | Shor et al.., 1965 | Shor et al.., 1965 | 20 | 6 | 120 |
| 1965 | Vancouver Island, British Columbia - strike line | White et al., 1985 | White et al., 1985 | 2 | 200 | 400 |
| 1967 | USGS Western US | Prodehl, 1979 | Prodehl, 1979 | 3 | 20 | 60 |
| 1969 | Washington and British Columbia backarc | Johnson and Couch, 1970 | Johnson and Couch, 1970 | 1 | 15 | 15 |
| 1976 | Oroville, California | Spieth and Hill, 1977 | Spieth et al., 1981 | 6 | 70 | 420 |
| 1978 | Mount Hood, Oregon | Kohler et al., 1987; Murphy, 2000 | Kohler et al., 1982 | 13 | 120 | 1560 |
| 1980 | Vancouver Island transect | Ellis et al., 1983 | Spence et al., 1985 | 5000 | 8 | 40000 |
| 1980 | Geysers, California | Janice Murphy, writt. comm., 2000 | | 5 | 120 | 600 |
| 1981 | Mount Shasta, California | Kohler et al., 1987 | Zucca et al., 1986 Fuis et al., 1987 | 14 | 120 | 1680 |
| 1982 | Mount Shasta, California | Kohler et al., 1987 | Zucca et al., 1986 Fuis et al., 1987 | 13 | 120 | 1560 |
| 1984 | Columbia Plateau, Washington | Catchings and Mooney, 1988 | Catchings and Mooney, 1988 | 4 | 240 | 960 |
| 1984 | Newberry volcano, Oreogn | Dawson and Stauber, 1986 | | 19 | 120 | 2280 |
| 1984 | East-Central Oregon E-W transect | Catchings and Mooney, 1988 | Catchings and Mooney, 1988 | 6 | 120 | 720 |
| 1985 | Medicine Lake, Oregon | Berge et al., 1986 | | 8 | 120 | 960 |
| 1988 | Columbia Plateau, Washington | Jarchow et al., 1991 | Jarchow et al., 1993, 1994 | 25 | 120 | 3000 |
| 1989 | Southern Cordillera, British Colubmia | Zelt et al., 1989 | Zelt, 1994; Clowes et al., 1995 | 25 | 200 | 5000 |

| | | | | | | |
|---|---|---|---|---|---|---|
| 1989 | Newport, Oregon transect | Trehu and Nakamura, 1993; Brocher et al., 1993 | Trehu et al., 1994 | 1925 | 16 | 30800 |
| 1990 | Southern Cordillera, British Colubmia | Brian Roberts, writt. comm., 2018 | Clowes et al., 1995 | 6 | 500 | 3000 |
| 1991 | N-S and E-W refraction lines, Washington and Oregon | Luetgert et al., 1993; Trehu et al., 1993 | Miller et a.., 1997 | 25 | 500 | 12500 |
| 1993 | Mendocino triple junction, California | Godfrey et al., 1995 | Beaudoin et al., 1996 | 29 | 560 | 16240 |
| 1994 | Mendocino triple junction, California | | Godfrey et al., 1998 | 36800 | 555 | 20424000 |
| 1994 | Cape Blanco, Oregon | Brocher et al., 1995 | | 12283 | 20 | 245660 |
| 1995 | Grays Harbor transect, Washington | Tom Parsons, writt. comm., 2000 | Parsons et al., 1998 | 31 | 1580 | 48980 |
| 1996 | Oregon and Washington margins | Flueh and Fisher, 1996 | Flueh et al., 1998; Gerdom et al., 2000 | 39580 | 165 | 6530700 |
| 1998 | Puget Lowland, Washington, and Georgia Strait, British Columbia | Brocher et al., 1999 | Brocher et al., 2001; Van Wagoner et al., 2002; Preston et al., 2003; Ramachandran et al., 2004, 2005, 2006 | 29000 | 288 | 8352000 |
| 1999 | Seattle Basin, Washington | Brocher et al., 2000 | Snelson et al., 2007 | 30 | 1003 | 30090 |
| 2000 | Seattle, Washington | Brocher et al., 2002 | Snelson et al., 2007 | 5 | 203 | 1015 |
| 2002 | Georgia Basin, British Columiba | Brocher et al., 2003 | Dash et al., 2007 | 10000 | 48 | 480000 |
| 2012 | Washington continental rise | Anne Trehu, written comm., 2018 | | 16300 | 6 | 97800 |
| 2012 | Ridge2Trench, Oregon and Washington | ShouShou Han, written comm., 2018; Anne Trehu, written comm., 2018 | Horning et al., 2016 | 32000 | 90 | 2880000 |
| 2014 | Mount Saint Helens, Washington | Eric Kiser, written comm., 2018 | Kiser et al., 2016 | 24 | 6505 | 156120 |
| **2020** | **Total number of raypaths (1960-2014)** | | | | | **39371190** |

*Table A-5: Active-source experiments along the Cascadian Subduction Zone since 1960*

| Year | Authors | MENA | MENI | MENII | MENDO | MCKSH | SN | TA/FA | 2D/3D | Method | Error |
|---|---|---|---|---|---|---|---|---|---|---|---|
| 1992 | Benz, Zandt, and Oppenheimer | | | | | | X | | 3D | Aki et al (1977) and Ellsworth and Koyanagi (1977) | 50 ms |
| 1994 | Beaudoin, Magee, and Benz | | | | | X | | | N/A | N/A | 70-125 ms |
| 1995 | Trehu and Mendo Working Group | X | X | X | X | X | | | N/A | N/A | N/A |
| 1996 | Beaudoin et al. | | X | | | | | | 2D | Hole (1992) | N/A |
| 1997 | Godfrey et al. | | X | | | | | | 2D | Hole (1992) | 118 ms |
| 1997 | Henstock, Levander, and Hole | | X | X | X | | | | 2D | Zelt and Smith (1992) | N/A |
| 1998 | Beaudoin et al. | | X | | | | | | 2D | Hole (1992) and Hole and Zelt (1995) | 82 ms |
| 1998 | Hole, Beaudoin, and Henstock | X | | X | X | | | | N/A | N/A | N/A |
| 2000 | Henstock and Levander | | X | | X | | | | 2D | Zelt and Smith (1992) | 140 ms |
| 2000 | Hole, Beaudoin, and Klemperer | X | | X | X | | | | 3D | Hole (1992) | N/A |
| 2003 | Henstock and Levander | | | X | X | | | | 2D | Zelt and Smith (1992) | 130 ms |
| 2009 | Thurber et al. | | | | | | X | | 3D | Zhang et al., (2004) , Zhang and Thurber, (2006) | 208 ms |
| 2010 | Eakin et al. | | | | | | | X | N/A | N/A | N/A |
| 2012 | Liu et al. | | | | | | X | X | 3D | Hermmann and Ammonn (2002) | N/A |
| 2015 | Chen, Zhao, and Wu | | | | | | X | X | 3D | Zhao (1992, ray tracing)Zhao (1994) and Zhao (2012, for tomography) | 412 ms |

*Table A-6: Compilation of previous imaging studies in the region, data utilization, and error if reported. "SN" denotes seismic networks, i.e., PNSN, BDSN, NCSN. "TA" and "FA" denote the Transportable and Flexible Arrays, respectively.*

<u>Additional Experiment Metadata</u>
MENII-WA2

| Station | Station No. | UTM Easting (m) | UTM Northing (m) | Elevation (km) |
|---------|-------------|-----------------|------------------|----------------|
| 2001 | 7091 | 435311 | 4389721 | 0.240 |
| 2002 | 7281 | 442573 | 4390781 | 0.473 |
| 2003 | 7294 | 452502 | 4385606 | 0.529 |
| 2004 | 7282 | 460821 | 4393086 | 0.738 |
| 2005 | 7116 | 470184 | 4395748 | 0.320 |
| 2006 | 7113 | 477793 | 4398658 | 0.554 |
| 2007 | 7112 | 493402 | 4405123 | 0.914 |
| 2008 | 7114 | 501323 | 4407756 | 1.126 |

*Table A-7: Additional wide-angle line from 1994 MENII survey, placed coast-perpendicular north of the MTJ*

MENII-WA8

| Station | Instrument No. | UTM Easting (m) | UTM Northing (m) | Elevation (km) |
|---------|----------------|-----------------|------------------|----------------|
| 8010 | 7114 | 413105 | 4595735 | 0.049 |
| 8020 | 7112 | 418765 | 4597749 | 0.229 |
| 8030 | 7107 | 423627 | 4598400 | 0.914 |
| 8040 | 7109 | 429688 | 4600423 | 1.033 |
| 8050 | 7108 | 436397 | 4600740 | 1.390 |
| 8060 | 6115 | 442960 | 4602835 | 1.487 |
| 8070 | 6109 | 447760 | 4603828 | 0.634 |
| 8080 | 6114 | 453505 | 4599475 | 0.829 |
| 8090 | 6111 | 456813 | 4603671 | 0.268 |
| 8100 | 6112 | 461088 | 4608034 | 0.366 |

*Table A-8:  Another wide-angle line from 1994 MENII survey, placed coast-perpendicular but south of the MTJ*

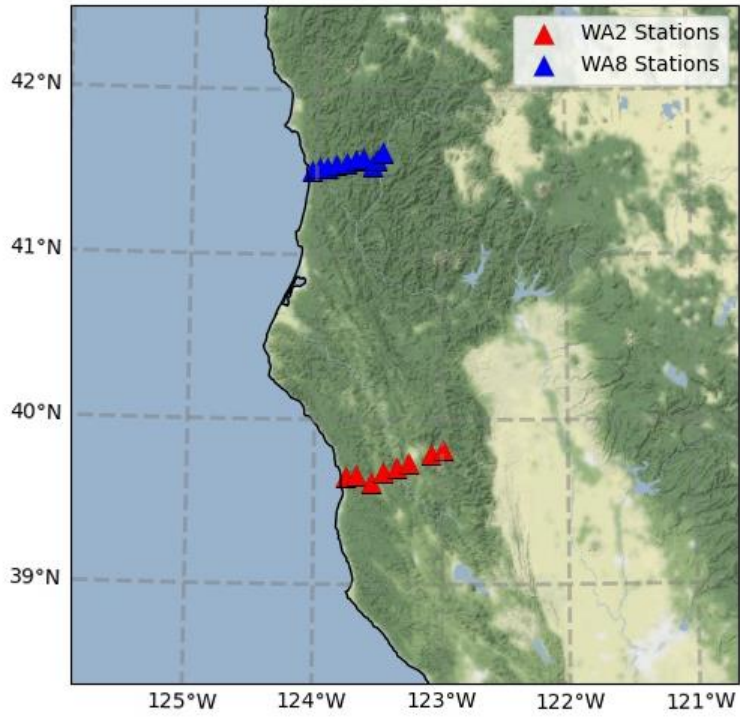Shot / Receiver Geometry for 1994 New Wide-Angle Lines WA2



*Figure A-7: Shot / Receiver geometry for the new (not reoccupied from 1993) wide-angle lines added in the 1994 MENII survey*

# REFERENCES CITED

Amante, C., and B. W. Eakins (2009), ETOPO1 1 Arc-Minute Global Relief Model: Procedures, Data Sources and Analysis, Natl. Geophys. Data Center, NESDIS, NOAA, U.S. Dept. Commerce, Boulder, Colo.

Barry, K. M., Cavers, D. A. and Kneale, C. W., 1975, Report on recommended standards for digital tape formats: Geophysics, 40, no. 02, 344-352.

Beaudoin, B. C., Godfrey, N. J., Klemperer, S. L., Lendl, C., Trehu, A. M., Henstock, T. J., Levander, A., Holl, J. E., Meltzer, A., S., Luetger, J. H., Mooney, W., D. (1996). Transition from slab to slabless: Results from the 1993 Mendocino triple junction seismic experiment. *Geology* ; 24 (3): 195–199. doi: https://doi.org/10.1130/0091-7613(1996)024<0195:TFSTSR>2.3.CO;2

Beaudoin, B. C., Hole, J. A., Klemperer, S. L., & Trehu, M. (1998). Results from seismic profiling and gravity, *103*(98), 30101–30115. https://doi.org/10.1029/98JB02231.

Bodmer, M., Toomey, D. R., Hooft, E. E. E., & Schmandt, B. (2018). Buoyant Asthenosphere Beneath Cascadia Influences Megathrust Segmentation. *Geophysical Research Letters*, 6954–6962. https://doi.org/10.1029/2018GL078700

Brocher, T. M., Parsons, T., Trehu, A. M., Snelson, C. M., & Fisher, M. A. (2003). Seismic evidence for widespread serpentinized forearc upper mantle along the Cascadia margin. *Geology*, *31*(3), 267–270. https://doi.org/10.1130/0091-7613(2003)031<0267:SEFWSF>2.0.CO;2

Brudzinski, M. R., & Allen, R. M. (2007). Segmentation in episodic tremor and slip all along Cascadia. *Geology*, *35*(10), 907. https://doi.org/10.1130/G23740A.1

Canales, J. P., Carbotte, S. M., Nedimovic, M. R., & Carton, H. (2017). Dry Juan de Fuca slab revealed by quantification of water entering Cascadia subduction zone. *Nature Geoscience*, *10*(11), 864–870. https://doi.org/10.1038/NGEO3050

Chaytor, J. D., Goldfinger, C., Dziak, R. P., & Fox, C. G. (2004). Active deformation of the Gorda plate: Constraining deformation models with new geophysical data. *Geology*, 32(4), 353- 356.

Clubb, F. J., Mudd, S. M., Hurst, M. D., & Grieve, S. W. D. (2019). Differences in channel and hillslope geometry record a migrating uplift wave at the Mendocino triple junction, California, USA. *Geology*, *XX*(Xx), 1–5. https://doi.org/10.1130/G46939.1

DeFelipe, I., Alcalde, J., Ivandic, M., Martí, D., Ruiz, M., Marzán, I., Diaz, J., Ayarza, P., Palomeras, I., Fernandez-Turiel, J.-L., Molina, C., Bernal, I., Brown, L., Roberts, R., and Carbonell, R.: Reassessing the lithosphere: SeisDARE, an open-access seismic data repository, Earth Syst. Sci. Data, 13, 1053–1071, https://doi.org/10.5194/essd-13-1053-2021, 2021.

Divins, D. L. (2003), Total Sediment Thickness of the World's Oceans & Marginal Seas, NOAA Natl. Geophys. Data Cent., Boulder, Colo.

Dziak, R. P., Fox, C. G., Bobbitt, A. M., & Goldfinger, C. (2001). Bathymetric map of the Gorda plate: Structural and geomorphological processes inferred from multibeam surveys. *Marine Geophysical Research*, 22(4), 235-250.

Eakin, C. M., Obrebski, M., Allen, R. M., Boyarko, D. C., Brudzinski, M. R., & Porritt, R. (2010). Seismic anisotropy beneath Cascadia and the Mendocino triple junction: Interaction of the subducting slab with mantle flow. *Earth and Planetary Science Letters*, 297(3), 627- 632.

Ferragut, G. (2021). MTJ (Version 1.0) [GitHub repository]. https://doi.org/10.5281/zenodo.5363562

Flueh, E. R., et al. (1998), New seismic images of the Cascadia subduction zone from cruise SO108—ORWELL, Tectonophysics, 293, 69–84.

Freymueller, Jeffrey T., et al. "Kinematics of the Pacific-North America plate boundary zone, northern California." *Journal of Geophysical Research: Solid Earth* 104.B4 (1999): 7419- 7441.

Furlong, K.P., 1993. Thermal-rheological evolution of the upper mantle and the development of the San Andreas fault system. In: M.J.R. Wortel, U. Hansen and R. Sabadini (Editors), Relationships between Mantle Processes and Geological Processes at or near The Earth' s Surface. *Tectonophysics*, 223: 149-164.

Furlong, K. P., & Govers, R. (1999). Ephemeral crustal thickening at a triple junction: The Mendocino crustal conveyor. *Geology*, 27(2), 127–130. https://doi.org/10.1130/0091-7613(1999)027<0127:ECTAAT>2.3.CO;2

Furlong, K. P., & Schwartz, S. Y. (2004). Influence of the Mendocino Triple Junction on the Tectonics of Coastal California. *Annual Review of Earth and Planetary Sciences*, 32(1), 403–433. https://doi.org/10.1146/annurev.earth.32.101802.120252

Furlong, K. P. (2014). Constraining the Crustal Conveyor : EarthScope Imaging of Mendocino Triple Constraining the Crustal Conveyor : EarthScope Imaging of Mendocino Triple Junction Tectonics, (May). https://doi.org/10.1130/B25885.1

Gao, Haiying (2018). "Three-dimensional variations of the slab geometry correlate with earthquake distributions at the Cascadia subduction system." *Nature Communications* 9.1 (2018): 1204.

GMT 6**:** Wessel, P., Luis, J. F., Uieda, L., Scharroo, R., Wobbe, F., Smith, W. H. F., & Tian, D. (2019). The Generic Mapping Tools version 6. *Geochemistry, Geophysics, Geosystems*, 20, 5556–5564. https://doi.org/10.1029/2019GC008515

Godfrey, N. J., Beaudoin, B. C., & Klemperer, S. L. (1997). Ophiolitic basement to the Great Valley forearc basin, California, from seismic and gravity data: Implications for crustal growth at the North American continental margin. *Geological Society of America Bulletin*, 109(12), 1536- 1562.

Goes, S., Govers, R., Schwartz ', S., Furlong, K., & Keck, ' W M. (1997). *EPSL Three-dimensional thermal modeling for the Junction area Mendocino Triple*. *Earth and Planetary Science Letters* (Vol. 148).

Gong, J., & McGuire, J. J. (2018). Interactions between strike-slip earthquakes and the subduction interface near the Mendocino Triple Junction. *Earth and Planetary Science Letters*, 482, 414-422.

Goldfinger, C., Grijalva, K., Bürgmann, R., Morey, A. E., Johnson, J. E., Nelson, C. H., … Gràcia, E. (2008). Late Holocene rupture of the northern San Andreas fault and possible stress linkage to the Cascadia Subduction Zone. In *Bulletin of the Seismological Society of America* (Vol. 98, pp. 861–889). https://doi.org/10.1785/0120060411

Gulick, Sean PS, Anne M. Meltzer, and Samuel H. Clarke. "Seismic structure of the southern Cascadia subduction zone and accretionary prism north of the Mendocino triple junction." *Journal of Geophysical Research: Solid Earth* 103.B11 (1998): 27207-27222.

Gulick, S. P. S., Meltzer, A. S., Henstock, T. J., & Levander, A. (2002). Internal deformation of the southern Gorda plate: Fragmentattion of a weak plate near the Mendocino triple junction. *Geology*, *29*(8), 691–694. https://doi.org/10.1130/0091-7613(2001)029<0691:IDOTSG>2.0.CO;2

Haberland, C., Rietbrock, A., Lange, D., Bataille, K. & Dahm, T. Structure of the seismogenic zone of the southcentral Chilean margin revealed by local earthquake traveltime tomograph. *J. Geophys. Res.* **114,** B01317 (2009).

Hamilton, E. L. (1979), $V_P/V_S$ and Poisson's ratios in marine sediments and rocks, J. Acoust. Soc. Am., 66, 1093–1101.

Hayes, G.P. and Furlong, K.P. (2007), Abrupt changes in crustal structure beneath the Coast Ranges of northern California – developing new techniques in receiver function analysis. Geophysical Journal International, 170: 313-336. https://doi.org/10.1111/j.1365-246X.2007.03401.x

Henstock, T. J., Levander, A., & Hole, J. A. (1997). Deformation in the lower crust of the San Andreas fault system in northern California. 33 (5338), 650-653.

Henstock, T. J., A. Levander, A. S. Meltzer, and S. P. S. Gulick, Deforma- tion and mass transfer at the Mendocino Triple Junction: What Gorda gives up, North America receives, Seismol. Res. Lett., 70, 246, 1999.

Henstock, T. J., and A. Levander, Lithospheric evolution in the wake of the Mendocino Triple Junction: Structure of the San Andreas Fault system at 2 Ma, *Geophys. J. Int.*, 140, 233– 247, 2000.

Henstock, T. J. (2003). Structure and seismotectonics of the Mendocino Triple Junction , California Structure and seismotectonics of the Mendocino Triple Junction , California, (May). https://doi.org/10.1029/2001JB000902

Hole, J. A., Beaudoin, B. C., & Klemperer, S. L. (2000). Vertical extent of the newborn San Andreas fault at the Mendocino triple junction. *Geology*, *28*(12), 1111. https://doi.org/10.1130/0091-7613(2000)28<1111:VEOTNS>2.0.CO;2

Horning, G., Canales, J. P., Carbotte, S. M., Han, S., Carton, H., Nedimović, M. R., & van Keken, P. E. (2016). A 2-D tomographic model of the Juan de Fuca plate from accretion at axial seamount to subduction at the Cascadia margin from an active source ocean bottom seismometer survey. *Journal of Geophysical Research: Solid Earth*, *121*(8), 5859–5879. https://doi.org/10.1002/2016JB013228

Hwang, L. J., Ahern, T., Ebinger, C. J., Ellsworth, W. L., Euler, G. G., Okal, E. A., Okubo, P. G., Walter, W. R. (2020). Rescuing Legacy Seismic Data FAIR'ly. *Seismological Research Letters*; 91 (3): 1339–1340. doi: https://doi.org/10.1785/0220200027

Krohe, A., (2017). The Franciscan Complex (California, USA) – The model case for return-flow in a subduction channel put to the test, *Gondwana Research*, Volume 45, P. 282-307, https://doi.org/10.1016/j.gr.2017.02.003.

Krischer, L., Megies, T., Barsch, R., Beyreuther, M., Lecocq, T., Caudron, C., Wassermann, J. (2015). ObsPy: A bridge for seismology into the scientific Python ecosystem. *Comput. Sci. Disc.* **8** 014003

Lock, J., Kelsey, H., Furlong, K., & Woolace, A. (2006). Late Neogene and Quaternary landscape evolution of the northern California Coast Ranges: Evidence for Mendocino triple junction tectonics. *Bulletin of the Geological Society of America*, *118*(9–10), 1232–1246. https://doi.org/10.1130/B25885.1

Materna, K., Taira, T. A., & Bürgmann, R. (2018). Aseismic Transform Fault Slip at the Mendocino Triple Junction From Characteristically Repeating Earthquakes. *Geophys. Res. Lett.*, 45(2), 699-707.

McCrory, P. A., Blair, J. L., Oppenheimer, D. H., & Walter, S. R. (2004). Depth to the Juan de Fuca slab beneath the Cascadia subduction margin: A 3-D model for sorting earthquakes. US Department of the Interior, US Geological Survey.

Department of State. Broad Agency Announcement. (April 2021). *BAA-2021-001*. https://sam.gov/opp/e83810b9df4c4ffeb086f5680900f596/view

Oleskevich, D.A., Hyndman, R.D., and Wang, K. 1999, 'The updip and downdip limits to great subduction earthquakes: Thermal and structural models of Cascadia, south Alaska, SW Japan, and Chile', *Journal of Geophysical Research*, v. 104, no. B7, p. 14965–14991.

Paulatto, M., Laigle, M., Galve, A., Charvis, P., Sapin, M., Bayrakci, G., … Kopp, H. (2017). Dehydration of subducting slow-spread oceanic lithosphere in the Lesser Antilles, (May). https://doi.org/10.1038/ncomms15980

Peacock, S. M., & Hyndman, R. D. (1999). Hydrous minerals in the mantle wedge and the maximum depth of subduction thrust earthquakes. *Geophysical Research Letters*, *26*(16), 2517–2520. https://doi.org/10.1029/1999GL900558

Peng, Y., Dong, D., Yan, J., & Chen, W. (2017). Geodetic constraint on the motion of a slab window: Implication for the Mendocino Crustal Conveyor model. *Geophysical Research Letters*, *44*(14), 7187–7193. https://doi.org/10.1002/2017GL074149

Ryan, W.B.F., S.M. Carbotte, J.O. Coplan, S. O'Hara, A. Melkonian, R. Arko, R.A. Weissel, V. Ferrini, A. Goodwillie, F. Nitsche, J. Bonczkowski, and R. Zemsky (2009), Global Multi-Resolution Topography synthesis, Geochem. Geophys. Geosyst., 10, Q03014, doi: 10.1029/2008GC002332

Schmalzle, G. M., McCaffrey, R., & Creager, K. C. (2014). Central Cascadia subduction zone creep. *Geochemistry, Geophysics, Geosystems*, *15*(4), 1515–1532. https://doi.org/10.1002/2013GC005172

Stone, I., Vidale, J. E., Han, S., & Roland, E. (2018). Catalog of Offshore Seismicity in Cascadia: Insights Into the Regional Distribution of Microseismicity and its Relation to Subduction Processes. *Journal of Geophysical Research: Solid Earth*, *123*(1), 641–652. https://doi.org/10.1002/2017JB014966

Toomey, D. R., et al. (2014), The Cascadia Initiative: A sea change in seismological studies of subduction zones, Oceanography, 27, 138–150.

Trehu, A.M., I., Asudeh, T. M. Brocher, J. H. Luetgert, W. D. Mooney, and J. L. Nabelek, Crustal architecture of the Cascadia forearc, Science, 266, 237-242, 1994

Trehu, A. M., and Mendocino Working Group (1995), Pulling the rug out from under California: Seismic images of the Mendocino Triple Junction Region, *Eos Trans. AGU*, 76(38), 369– 381

Vanderbeek, B. P. (2019). Pn Tomography of the Juan de Fuca and Gorda Plates : Implications for Mantle Deformation and Hydration in the Oceanic Lithosphere Journal of Geophysical Research : Solid Earth, 8565–8583. https://doi.org/10.1029/2019JB017707

Velasco, A. A., C. J. Ammon, and T. Lay, 1994, Recent large earthquakes near Cape Mendocino and in the Gorda plate: Broadband source time functions, fault orientations, and rupture complexities, *J. Geophys. Res*., 99, 711-728.

Wilson, D.S. 2002, 'The Juan de Fuca plate and slab: Isochron structure and Cenozoic plate motions', *U.S. Geological Survey Open File Report*, v. 02P328, p. 9–12.